J|A|C|S ARTICLES

Published on Web 11/05/2010

Linking Local Environments and Hyperfine Shifts: A Combined Experimental and Theoretical ^{31}P and ^{7}Li Solid-State NMR Study of Paramagnetic Fe(III) Phosphates

Jongsik Kim,[†] Derek S. Middlemiss,[†] Natasha A. Chernova,[‡] Ben Y. X. Zhu,[†] Christian Masquelier,[§] and Clare P. Grey*[,†,||]

Department of Chemistry, Stony Brook University, Stony Brook, New York 11794-3400, United States, Department of Chemistry, University of Cambridge, Lensfield Road, Cambridge, United Kingdom CB2 1EW, Institute for Materials Research, SUNY Binghamton, Binghamton, New York 13902-6000, United States, and Laboratoire de Réactivité et Chimie des Solides, UMR CNRS 6007, Université de Picardie Jules Verne, 80039 Amiens, France

Received March 30, 2010; E-mail: cpg27@cam.ac.uk

Abstract: Iron phosphates ($FePO_4$) are among the most promising candidate materials for advanced Li-ion battery cathodes. This work reports upon a combined nuclear magnetic resonance (NMR) experimental and periodic density functional theory (DFT) computational study of the environments and electronic structures occurring in a range of paramagnetic Fe(III) phosphates comprising $FePO_4$ (heterosite), monoclinic $Li_3Fe_2(PO_4)_3$ (anti-NASICON A type), rhombohedral $Li_3Fe_2(PO_4)_3$ (NASICON B type), $LiFeP_2O_7$, orthorhombic $FePO_4 \cdot 2H_2O$ (strengite), monoclinic $FePO_4 \cdot 2H_2O$ (phosphosiderite), and the dehydrated forms of the latter two phases. Many of these materials serve as model compounds relevant to battery chemistry. The ^{31}P spin−echo mapping and ^{7}Li magic angle spinning NMR techniques yield the hyperfine shifts of the species of interest, complemented by periodic hybrid functional DFT calculations of the respective hyperfine and quadrupolar tensors. A Curie−Weiss-based magnetic model scaling the DFT-calculated hyperfine parameters from the ferromagnetic into the experimentally relevant paramagnetic state is derived and applied, providing quantitative finite temperature values for each phase. The sensitivity of the hyperfine parameters to the composition of the DFT exchange functional is characterized by the application of hybrid Hamiltonians containing admixtures 0%, 20%, and 35% of Fock exchange. Good agreement between experimental and calculated values is obtained, provided that the residual magnetic couplings persisting in the paramagnetic state are included. The potential applications of a similar combined experimental and theoretical NMR approach to a wider range of cathode materials are discussed.

1. Introduction

Motivated by the promising performance of olivine-type $LiFePO_4$ as a candidate Li-ion battery cathode material,[1−5] various Fe(III) phosphate compounds such as $Li_3Fe_2(PO_4)_3$, $Fe_4(P_2O_7)_3$, $FePO_4$, $LiFeP_2O_7$, etc., have been synthesized and characterized in regard to their structural and electrochemical properties.[2,6−13] Methods such as particle size control[3] and surface coating with conductive carbon[4,5,14−16] have been reported to improve the electrochemical performance of such materials. Polymorphic hydrated forms of Fe(III) phosphates, $FePO_4 \cdot nH_2O$ ($n \approx 2$), have also been considered as Li battery positive electrodes, permitting reversible reduction to approximately 90% of their theoretical capacities in the 2−4 V range vs Li^+/Li,[17−20] where this nomenclature denotes a potential relative to a Li-metal negative electrode. However,

[†] Stony Brook University.
[‡] SUNY Binghamton.
[§] Université de Picardie Jules Verne.
[||] University of Cambridge.

(1) Anderson, A. S.; Thomas, J. O. *J. Power Sources* **2001**, *97*−*98*, 498.
(2) Padhi, A. K.; Nanjundaswamy, K. S.; Goodenough, J. B. *J. Electrochem. Soc.* **1997**, *144*, 1188.
(3) Yamada, A.; Chung, S. C.; Hinokuma, K. *J. Electrochem. Soc.* **2001**, *148*, A224.
(4) Armand, M.; Gauthier, M.; Magnan, J.-F.; Ravet, N. World Patent WO 02/27823 A1, 2002.
(5) Ravet, N.; Goodenough, J. B.; Besner, S.; Simoneau, M.; Hovington, P.; Armand, M. *196th Meeting of the Electrochemical Society*; Honolulu, HI, 1999; Abstract 127.
(6) Padhi, A. K.; Nanjundaswamy, K. S.; Masquelier, C.; Goodenough, J. B. *J. Electrochem. Soc.* **1997**, *144*, 2581.
(7) Song, Y.; Zavalij, P. Y.; Suzuki, M.; Whittingham, M. S. *Inorg. Chem.* **2002**, *41*, 5778.
(8) Wurm, C.; Morcrette, M.; Rousse, G.; Dupont, L.; Masquelier, C. *Chem. Mater.* **2002**, *14*, 2701.
(9) Rousse, G.; Rodriguez-Carvajal, J.; Wurm, C.; Masquelier, C. *Solid State Sci.* **2002**, *4*, 973.
(10) Rousse, G.; Rodriguez-Carvajal, J.; Patoux, S.; Masquelier, C. *Chem. Mater.* **2003**, *15*, 4082.
(11) Patoux, S.; Wurm, C.; Morcerette, M.; Rousse, G.; Masquelier, C. *J. Power Sources* **2003**, *119*−*121*, 278.
(12) Masquelier, C.; Wurm, C.; Rodriguez-Carvajal, J.; Gaubicher, J.; Nazar, L. *Chem. Mater.* **2000**, *12*, 525.
(13) Zaghib, K.; Julien, C. M. *J. Power Sources* **2005**, *142*, 279.
(14) Huang, H.; Yin, S.-C.; Nazar, L. F. *Electrochem. Solid-State Lett.* **2001**, *4*, A170.
(15) Chen, Z.; Dahn, J. R. *J. Electrochem. Soc.* **2002**, *149*, A1184.
(16) Yamada, A.; Hosoya, M.; Chung, S.-C.; Kudo, Y.; Hinokuma, K.; Liu, K.-Y.; Nishi, Y. *J. Power Sources* **2003**, *119*−*121*, 232.
(17) Delacourt, C.; Poizot, P.; Bonnin., D.; Masquelier, C. *J. Electrochem. Soc.* **2009**, *156*, A595.

the electrochemical capacities of the dehydrated orthorhombic (DH strengite) and monoclinic (DH phosphosiderite) $FePO_4$ polymorphs fall significantly below that of the heterosite and amorphous forms.[7,17,18] Meanwhile, the monoclinic (A type, anti-NASICON) and rhombohedral (B type, NASICON) forms of $Li_3Fe_2(PO_4)_3$[1,21,22] permit for reversible insertion of approximately two Li per formula unit at approximately 2.8 V vs Li^+/Li.[21] Common to all of these phases is the suggestion that the covalency of the Fe−O and P−O bonds plays an important role in controlling the Fe redox potential,[23,24] the magnitude of this so-called 'inductive' effect being sensitive both to the crystal structure and to the nature of the anion or polyanion (O, PO_4, SiO_4, SO_4, P_2O_7, etc.). Attempts to improve the electrochemical performance of such cathodes have included syntheses of more disordered materials featuring, for example, mixed phosphate−silicate polyanion sublattices, Li^+-Fe^{2+} exchange, and substitution of various transition metal (TM) cations.[25−28]

Achieving a more complete description of the lattice and electronic structures of cathode materials at the atomic level remains a key challenge, driven by the need both to rationalize and to learn how to engineer favorable electrochemical properties. In particular, insight is sought into the actual environments experienced by dopant and electrochemically active species, as opposed to the more average structures often provided by conventional diffraction techniques. NMR-based characterizations confer definite advantages in this regard, especially in light of the fact that many such phases may show inherent structural disorder or may develop such upon partial delithiation. Previous successful NMR studies within the field include the characterization of local structure in mixed TM spinels such as $LiNi_xMn_{2-x}O_4$[29] and rock-salt-derived layered compounds such as $Li[Li_{1/9}Ni_{3/9}Mn_{5/9}]O_2$,[30,31] particle isolation effects and power fading in $Li[Ni_{0.8}Co_{0.15}Al_{0.05}]O_2$ electrodes,[32] and identification of cation orderings in layered $Li[Ni_xMn_xCo_{1-2x}]O_2$ phases.[33]

NMR studies suffer the additional complication that many cathode materials display paramagnetism associated with unpaired TM d electrons at typical battery operating temperatures. Beyond the technical difficulties this raises in terms of obtaining sufficient spectral resolution, there remains the urgent need to more fully characterize the empirical relationships linking hyperfine NMR shifts to their originating local environments. The present study addresses the latter point for ^7Li and ^{31}P sites within a range of paramagnetic Fe(III) phases. Moreover, our related research regards Fe(III)PO_4 compounds as models relevant to the adsorption of phosphate ions upon the surfaces of environmentally important iron oxyhydroxides (FeOOH) such as goethite and ferrihydrite.[34−39] The present results, spanning a range of Fe−O−P bond path geometries, will assist in determining the sites at and coordination modes with which phosphate ions bind to such materials.[40]

Here we present a combined experimental and theoretical ^7Li and ^{31}P NMR study of a range of Fe(III) phosphate materials: $FePO_4$ (heterosite type), monoclinic $Li_3Fe_2(PO_4)_3$ (A type; anti-NASICON), rhombohedral $Li_3Fe_2(PO_4)_3$ (B type; NASICON), $LiFeP_2O_7$, orthorhombic $FePO_4 \cdot 2H_2O$ (strengite), monoclinic $FePO_4 \cdot 2H_2O$ (phosphosiderite), and the DH forms of the latter two materials. Our approach is novel in the extent of the comparisons that it affords between experimental and theoretical NMR parameters for paramagnetic solids, particularly in light of the range of materials considered, and in the use of hybrid DFT functionals. Two complementary techniques are employed: first, the NMR spectra are analyzed in terms of simple crystallographic considerations, seeking to relate the geometries of the various Fe−O−P/Li bond paths to the respective hyperfine shifts. Second, theoretical hyperfine and quadrupolar coupling parameters for all relevant sites are obtained directly from periodic density functional theory (DFT) calculations. Our aim here, uncommon in periodic calculations, is to provide quantitatively accurate shifts, proceeding beyond the methods applied in previous pseudopotential-based studies of TM oxide Li cathode phases.[41] The earlier calculations did not access the spin densities at nuclear positions and so could offer only a qualitative interpretation of experimental shifts based upon the integration of spin densities over approximate Li ionic volumes.[41] The present study builds upon this approach, deploying an all-electron treatment including variationally free core states, hybrid exchange-correlation potentials beyond the pure density functionals previously applied,[41] and an empirical model of the finite temperature paramagnetic susceptibility. The latter turns out to be a particularly important factor, as shall be shown below.

The use of hybrid Hamiltonians bearing varying admixtures of nonlocal Fock exchange provides useful insight into the variations in hyperfine parameters with functional composition.

(18) Delacourt, C.; Wurm, C.; Reale, P.; Morcrette, M.; Masquelier, C. *Solid State Ionics* **2004**, *173*, 113.
(19) Reale, R.; Scrosati, B.; Delacourt, C.; Wurm, C.; Morcrette, M.; Masquelier, C. *Chem. Mater.* **2003**, *15*, 5051.
(20) Masquelier, C.; Reale, P.; Morcrette, M.; Wurm, C.; Dupont, L.; Larcher, D. J. *J. Electrochem. Soc.* **2002**, *149*, A1037.
(21) Masquelier, C.; Padhi, A. K.; Nanjundaswamy, K. S.; Goodenough, J. B. *J. Solid State Chem.* **1998**, *135*, 228.
(22) Rousse, G.; Rodriguez-Carvajal, J.; Wurm, C.; Masquelier, C. *Chem. Mater.* **2001**, *13*, 4527.
(23) Padhi, A. K.; Nanjundaswamy, K. S.; Masquelier, C.; Okada, S.; Goodenough, J. B. *J. Electrochem. Soc.* **1997**, *144*, 1609.
(24) Manthiram, A.; Goodenough, J. B. *J. Solid State Chem.* **1987**, *71*, 349.
(25) Hamelet, S.; Gibot, P.; Casas-Cabanas, M.; Bonnin, D.; Grey, C. P.; Cabana, J.; Leriche, J.-B.; Rodriguez-Carvajal, J.; Courty, M.; Levasseur, S.; Carlach, P.; Thournout, M. V.; Tarascon, J. M.; Masquelier, C. *J. Mater. Chem.* **2009**, *19*, 3979.
(26) Recham, N.; Casas-Cabanas, M.; Cabana, J.; Grey, C. P.; Jumas, J. C.; Dupont, L.; Armand, M.; Tarascon, J. M. *Chem. Mater.* **2008**, *20*, 6798.
(27) Yamada, A.; Chung, S. C. *J. Electrochem. Soc.* **2001**, *148*, A960.
(28) Gibot, P.; Casas-Cabanas, M.; Laffont, L.; Levasseur, S.; Carlach, P.; Hamelet, S.; Tarascon, J.; Masquelier, C. *Nat. Mater.* **2008**, *7*, 741.
(29) Lee, Y. J.; Eng, C.; Grey, C. P. *J. Electrochem. Soc.* **2001**, *148*, A249.
(30) Yoon, W.-S.; Kim, N.; Yang, X.-Q.; McBreen, J.; Grey, C. P. *J. Power Sources* **2003**, *119*, 649.
(31) Jiang, M.; Key, B.; Meng, Y. S.; Grey, C. P. *Chem. Mater.* **2009**, *21*, 2733.
(32) Kerlau, M.; Reimer, J. A.; Cairns, E. J. *Electrochem. Commun.* **2005**, *7*, 1249.
(33) Zeng, D.; Cabana, J.; Breger, J.; Yoon, W.-S.; Grey, C. P. *Chem. Mater.* **2007**, *19*, 6277.
(34) Cornell, R. M.; Schwertmann, U. *The Iron Oxides*; VCH: New York, 1996.
(35) Nowack, B.; Stone, A. T. *Water Res.* **2006**, *40*, 2201.
(36) Lin, S.-H.; Kao, H.-C.; Cheng, C.-H.; Juang, R.-S. *Colloids Surf., A* **2004**, *234*, 71.
(37) Strauss, R.; Brummer, G. W.; Barrow, N. J. *Eur. J. Soil Sci.* **1997**, *48*, 101.
(38) Deliyanni, E. A.; Peleka, E. N.; Lazaridis, N. K. *Sep. Purif. Technol.* **2007**, *52*, 478.
(39) Chitrakar, R.; Tezuka, S.; Sonoda, A.; Sakane, K.; Ooi, K.; Hirotsu, T. *J. Colloid Interface Sci.* **2006**, *298*, 602.
(40) Kim, J.; Li, W.; Phillips, B. L.; Chernova, N.; Grey, C. P. To be submitted.
(41) Carlier, D.; Menetrier, M.; Grey, C. P.; Delmas, C.; Ceder, G. *Phys. Rev. B* **2003**, *67*, 174103.

The DFT calculations are performed within the ferromagnetic state, the hyperfine data obtained then being scaled into the experimentally relevant paramagnetic regime by application of the Curie−Weiss-based magnetic model outlined below. Previous computational studies have not, to the best of our knowledge, considered such a scaling technique. Similarly motivated theoretical NMR studies have been applied to varying oxovanadium phosphates, but there the magnetic model involved the direct diagonalization of parametrized Heisenberg−Dirac−van-Vleck Hamiltonians.[42−44] The present approach is more straightforward and, subject to its successful use here, might be readily applied to the analysis of the paramagnetic NMR spectra of a broad range of TM compounds. Experimentally derived sets of Curie−Weiss parameters defining the temperature-dependent magnetic susceptibility $\chi(T)$ of each material are required. However, the $\chi(T)$ curves of strengite and phosphosiderite have not previously been reported and are therefore obtained and analyzed here.

The article is structured as follows: detailed descriptions of the relevant crystal structures are presented first as an aid to the subsequent analyses of the NMR spectra. Next, the NMR shift mechanisms relevant within the present paramagnetic Fe(III) phases are outlined, along with the theoretical method used to obtain the hyperfine parameters. The experimental methodology is then presented, followed by the combined experimental and theoretical results, associated discussion, and conclusions.

2. Crystal Structures

$FePO_4$ (heterosite type, space group *Pnma*) is an olivine-type compound,[24] the crystal structure[8] (Figure 1a) comprising FeO_6 octahedra and PO_4 tetrahedra linked such that each PO_4 unit shares a corner with four FeO_6 units and an edge with one further FeO_6 unit. A single P sublattice occurs within this material.

Monoclinic $Li_3Fe_2(PO_4)_3$ (A type; anti-NASICON; space group $P2_1/n$) is readily formed by the reaction of stoichiometric mixtures of Fe_2O_3 and LiH_2PO_4 at approximately 800 °C under air.[11,21,45] The structure comprises corner-sharing FeO_6 and PO_4 units (Figure 1b), with the Fe(III) ions distributed over two and the Li and P ions each over three symmetry-distinct sublattices.[11,45] The three P sites, denoted here as P1, P1s, and P2, each contact four Fe(III) ions, in keeping with the corner-sharing motif. The Li1 site is 4-fold coordinated, linking to two neighboring FeO_6 units by edge sharing, while the Li2 and Li3 sites are both 5-fold coordinated.[11] However, Li2 bears one Li−O bond of length 2.46 Å,[11] substantially longer than typical Li−O distances of approximately 1.7−2.0 Å. Similarly, the Li3 site displays two substantially elongated Li−O bonds of lengths 2.37 and 2.44 Å.[11]

Rhombohedral $Li_3Fe_2(PO_4)_3$ (B type; NASICON; space group $R\bar{3}$) is obtained by ion exchange from $Na_3Fe_2(PO_4)_3$, its framework comprising exclusively corner-sharing FeO_6 and PO_4 units (Figure 1c).[12,46] Here, the Fe(III) ions are distributed over two symmetry-distinct sublattices, while the Li and P ions each occupy a single sublattice. The PO_4 ions contact four and the Li ions (in tetrahedral LiO_4 coordination) three Fe(III) sites in their first cation coordination shells, the LiO_4 units displaying two corner-sharing and one edge-sharing contact with neighboring FeO_6 units.

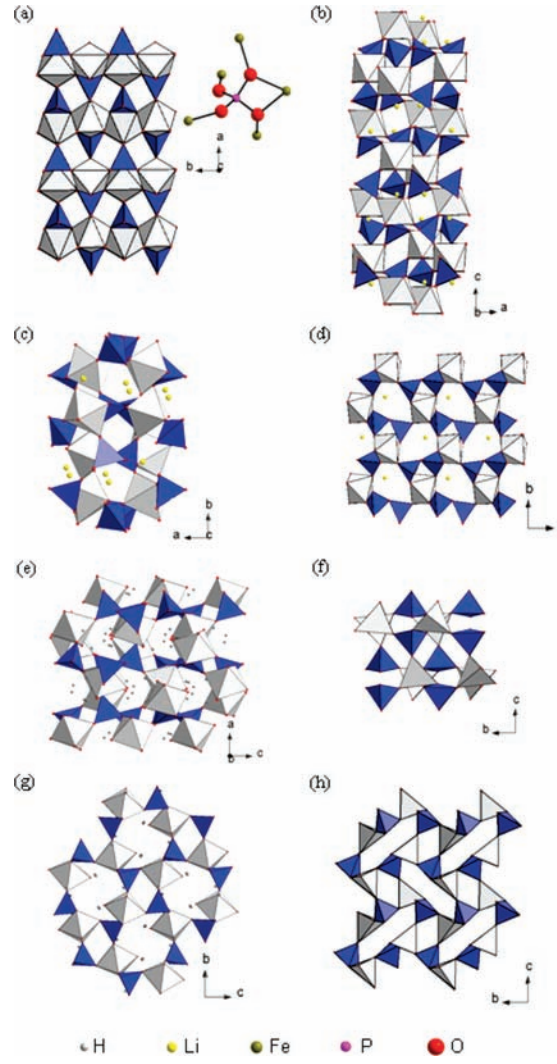

Figure 1. Crystal structures of (a) heterosite $FePO_4$, (b) monoclinic $Li_3Fe_2(PO_4)_3$, (c) rhombohedral $Li_3Fe_2(PO_4)_3$, (d) $LiFeP_2O_7$, (e) strengite, (f) DH strengite, (g) phosphosiderite, and (h) DH phosphosiderite. Inset in a: local environment of P ions. Crystal structures drawn in accord with the reported crystallographic parameters.[7,9−11,46]

The crystal structure of the $LiFeP_2O_7$ diphosphate is monoclinic (space group $P2_1$), as shown in Figure 1d.[8,9,47] Here, the Fe(III) and Li ions each occupy a single sublattice and the P ions two symmetry-distinct sublattices denoted P1 and P2. Each FeO_6 unit links to six P_2O_7 groups such that P ions contact three Fe(III) ions in their first cation coordination shells, linking to two Fe(III) ions by corner sharing and to the third by edge sharing split over both P ions in the P_2O_7 unit. The Li ions occupy tunnels formed by the FeO_6 and P_2O_7 units and contact two Fe(III) ions by edge sharing in their first cation coordination shells.

(42) Petit, S.; Borshch, S. A.; Robert, V. *J. Am. Chem. Soc.* **2003**, *125*, 3959.
(43) Petit, S.; Borshch, S. A.; Robert, V. *Inorg. Chem.* **2004**, *43*, 4210.
(44) Hairie, T.; Robert, V.; Petit, S. *Phys. Rev. B* **2006**, *74*, 052408.
(45) Bykov, A. B.; Chirkin, A. P.; Demyanets, L. N.; Doronin, S. N.; Genkina, E. A.; Ivanov-Shits, A. K.; Kondratyuk, I. P.; Maksimov, B. A.; MelÕnikov, O. K.; Muradyan, L. N.; Simonov, V. I.; Timofeeva, V. A. *Solid State Ionics* **1990**, *38*, 31.
(46) Andersson, A. S.; Kalska, B.; Jonsson, P.; Haggstrom, L.; Nordblad, P.; Tellgren, R.; Thomas, J. O. *J. Mater. Chem.* **2000**, *10*, 2542.
(47) Riou, D.; Nguyen, N.; Benloucif, R.; Raveau, B. *Mater. Res. Bull.* **1990**, *25*, 1363.

Strengite and phosphosiderite have the same stoichiometry $FePO_4 \cdot 2H_2O$, crystallizing in orthorhombic (space group *Pbca*) and monoclinic (space group $P2_1$) lattices, respectively (Figure 1e and 1g).[48] The structures of both polymorphs consist of corner-sharing FeO_6 and PO_4 units, two corners of each FeO_6 unit hosting the O atoms associated with structural water molecules. The PO_4 units contact four Fe(III) ions in their first cation coordination shells. Loss of structural water occurs when strengite is heated to 120 °C and when phosphosiderite is dried at 80 °C under vacuum, leading in both cases to the formation of distinct DH phases.[7,19] The FeO_6 octahedra are transformed to FeO_4 tetrahedra by this process, but the respective space group symmetries of the two forms remain unchanged (Figure 1f and 1h).[7] The Fe(III) coordination in DH phosphosiderite might reasonably be regarded as pseudotetrahedral, given the existence of an elongated fifth Fe−O bond of length 2.24 Å. However, FeO_4 and PO_4 units retain a corner-sharing motif, the P sites again contacting four Fe(III) ions in their first cation coordination shells.

3. Solid-State NMR of Paramagnetic Materials

3.1. Shift Mechanisms. Solid-state NMR spectroscopy is well established as offering a quantitative description of the local environments of NMR-active nuclei at the atomic level. However, only a limited number of successful NMR studies of Fe(III) phases exist, a scarcity largely due to the substantial line broadenings and NMR shifts experienced in paramagnetic systems.[49−51] Moreover, ^{31}P (nuclear spin quantum number $I = 1/2$) emerges as a particularly challenging species from which to obtain high-resolution NMR, as a consequence of both the increased shift due to the relatively large ^{31}P gyromagnetic ratio and the high degree of covalency of TM···P bond pathways (of Fe−O−P type in the present materials)[52−55] and of the difficulties inherent to the excitation of broad resonances. Meanwhile, the ^{7}Li ($I = 3/2$) NMR is further complicated by the potential contribution of both dipolar and quadrupolar interactions to the spinning sideband intensities. The latter two interactions may, in principle, be separated by comparing spectra obtained at two different fields, given that the former scales with the field while the latter is field independent. Alternatively, ^{6}Li spectra can be acquired, since this $I = 1$ nucleus possesses a much smaller quadrupole moment.

The large hyperfine shifts obtained in typical inorganic paramagnets may generally be ascribed to the Fermi contact (FC) interaction arising out of the delocalization of some fraction of the spin density nominally resident within the TM d orbitals into the s orbitals of the NMR observed site. The latter restriction reflects the fact that it is only s orbitals that manifest finite values at the nucleus. The contact NMR shift, δ_{iso} (ppm), is often predicted or rationalized on the basis of an expression of the form[56]

$$\delta_{iso} = \frac{10^6 \Delta\nu}{\nu_0} = \frac{10^6 A_{iso} \chi_M}{N_A \mu_0 g_e \mu_B g_I \mu_N} \quad (1)$$

where A_{iso} denotes the isotropic hyperfine coupling constant linking the unpaired TM electrons distributed throughout the lattice with the NMR observed nucleus, χ_M is the paramagnetic molar susceptibility of the compound studied, N_A is Avogadro's number, μ_0 is the permeability of free space, g_e is the electron g factor (assumed equal to the approximated free electron value of 2 hereafter), μ_B is the Bohr magneton, $\nu_0 = g_I \mu_N B_0/h$ denotes the single quantum resonance frequency of the observed nucleus, g_I and μ_N are the nuclear g factor and magneton, respectively, B_0 is the applied static magnetic induction, and h is Planck's constant.

It is clear that the contact shift varies directly with A_{iso}, which is in turn proportional to the electron spin density transferred from TM to ligand sites (more specifically, to the spin density present precisely at the NMR observed nucleus). In practice, this means that A_{iso}, displays a useful sensitivity to a range of factors defining the local environment of the observed nucleus, including the number, geometry, and degree of covalency of the bond pathways linking the paramagnetic and observed species.[41,50,57] The shift also varies directly with the paramagnetic susceptibility, χ_M, which is in turn sensitive to the number of unpaired electrons at and the nature of any residual magnetic correlations between the TM ions. Interestingly, it would seem that there has been little previous systematic study of the influence of such correlations upon calculated hyperfine parameters. Accordingly, both Curie−Weiss and Curie magnetic models are applied below: the former incorporates a mean field treatment of the correlations and the latter represents formally isolated TM moments.

Previous Mössbauer studies of diamagnetic ^{119}Sn dopants in a range of rare earth Fe(III) orthoferrites and Fe_2O_3 analyzed the spin density transfers arising due to various types of crystal-field-split orbital interactions.[58] Extending these models to the present materials and considering Fe−O−P/Li pathways at bond angle θ, we distinguish limiting linear and orthogonal cases as follows: (i) $\theta = 180°$ Fe(e_g)−O(pσ)−P/Li (delocalization type); (ii) $\theta = 180°$ Fe(t_{2g})−O(pπ p.e. pσ)−P/Li (polarization type); (iii) $\theta = 90°$ Fe(e_g)−O(pσ p.e. pπ)−P/Li (polarization type); and (iv) $\theta = 90°$ Fe(t_{2g})−O(pπ)−P/Li (delocalization type), where p.e. denotes an intra-atomic potential exchange (Hund's first rule type) interaction between electrons in O 2p orbitals and σ and π label orbitals relative to the Fe−O vector. The delocalization and polarization mechanisms are expected to transfer majority [i.e., positive, assuming the Fe(III) moments are also positive] and minority (negative) spin density, respectively, from Fe(III) to P/Li sites. However, the former paths are expected to dominate over the latter, given that they involve one and two intervening O orbitals, respectively.

It is difficult to predict the magnitude of the shift at intermediate angles, expressions for the hyperfine field at ^{119}Sn dopants, H_{hf} (in theory proportional to the contact NMR shift of eq 1), of the form

(48) Taxer, K.; Bartl, H. *Cryst. Res. Technol.* **2004**, *39*, 1080.
(49) Cole, K. E.; Paik, Y.; Reeder, R. J.; Schoonen, M.; Grey, C. P. *J. Phys. Chem. B* **2004**, *108*, 6938.
(50) Kim, J.; Nielsen, U. G.; Grey, C. P. *J. Am. Chem. Soc.* **2008**, *130*, 1285.
(51) Nielsen, U. G.; Paik, Y.; Julmis, K.; Schoonen, M. A. A.; Reeder, R. J.; Grey, C. P. *J. Phys. Chem. B* **2005**, *109*, 18310.
(52) Mali, G.; Ristic, A.; Kaucic, V. *J. Phys. Chem. B* **2005**, *109*, 10711.
(53) Canesson, L.; Tuel, A. *Chem. Commun.* **1997**, 241.
(54) Sananes, M. T.; Tuel, A. *J. Chem. Soc., Chem. Commun.* **1995**, 1323.
(55) Wilcke, S. L.; Lee, Y.-J.; Cairns, E. J.; Reimer, J. A. *Appl. Magn. Reson.* **2007**, *32*, 547.
(56) Bertini, I.; Luchinat, C.; Parigi, G. *Prog. Nucl. Magn. Reson. Spectrosc.* **2002**, *40*, 249.
(57) Grey, C. P.; Dupre, N. *Chem. Rev.* **2004**, *104*, 4493.
(58) Lyubutin, I. S.; Dmitrieva, T. V.; Stepin, A. S. *J. Expt. Theor. Phys.* **1999**, *88*, 590.

$$H_{hf}(\theta) = \alpha + \beta \cos\theta + \gamma \cos^2\theta \quad (2)$$

having been applied in the previous studies of Fe(III) oxides,[58−60] where α, β, and γ denote fitted coefficients. Here, the first term arises due to angularly independent Fe(d)−O(s) σ overlap, the second from angularly dependent Fe(d)−O(sp) σ overlap, and the third from angularly dependent Fe(d)−O(p) σ and π overlaps. The hyperfine field (and associated contact shift) approaches a minimum at $\theta = \cos^{-1}(-\beta/2\gamma)$ within the range $90° \leq \theta \leq 180°$. Lacking fitted α, β, and γ coefficients for the present phases we cannot be more specific but note instead that the previous ^{119}Sn Mössbauer study provided values of +949, +2487, and +1889 kOe, respectively, leading to a minimum at $\theta = 131°$.[58] It should be borne in mind, however, that the shift is always expected to be positive within the present materials and should generally increase with the number of Fe−O−P/Li bond pathways. Models for the distance dependence present greater difficulties, and so we adopt the straightforward notion that the elongation of the bonds comprising the Fe−O−P/Li pathways should result in weaker overlap and thus in smaller shifts.

While we note the considerable success of even very simple empirical models for the prediction of contact shifts,[29−32,61] clear difficulties remain, particularly in attempting to assign closely spaced shifts to sites with very similar local bonding environments. Accordingly, we now outline a quantitative periodic DFT-based method for the calculation of hyperfine parameters.

3.2. First-Principles Calculations and Model of the Paramagnetic State. All electronic structure calculations in this work were performed within the CRYSTAL06 linear combinations of atomic orbitals (LCAO) code.[62] Given that the reliable calculation of hyperfine parameters places heavy demands on basis set (BS) quality, two types of BS were adopted: the first is a more limited set amenable to structural optimizations (denoted BS-I hereafter) and the second an extended and more flexible set suitable for single-point hyperfine calculations (denoted BS-II). For BS-I, the individual atomic sets are of the form (4s1p)/[2s1p] for H, (7s2p1d)/[1s2sp1d] for Li, (10s4p1d)/[1s2sp1d] for O, (16s8p1d)/[1s3sp1d] for P, and (20s12p5d)/[1s4sp2d] for Fe, where the values in parentheses denote the number of Gaussian primitives and the values in square brackets the contraction scheme. The BS-I sets were selected from the CRYSTAL online repository:[63] the Fe set having previously been used in a wide range of magnetic Fe compounds, the H, O, and P sets in a recent study of hexagonal hydroxyapatite $Ca_{10}(PO_4)_6(OH)_2$,[64] and the Li set in LiOH.[65]

The BS-II sets were based upon those tested and deemed sufficiently accurate within a recent extensive set of EPR calculations for isolated TM complexes by Munzarová and Kaupp, albeit with adjustments for use in periodic calculations.[66] Modified IGLO-III sets[67] were adopted for H, O, and P, removing the most diffuse s and p shells in the latter two species and the most diffuse s shell in the former, yielding a (5s2p)/[3s2p] set for H, (10s6p2d)/[6s5p2d] for O, and (11s7p3d)/[7s6p3d] for P. Lacking a previously defined IGLO-III set for Li, a reasonably flexible and extended TZDP-derived (triple-ζ plus double-polarization) basis[68] was used in which the most diffuse s shell was removed and the exponents of the remaining outermost s shell and two outermost p shells increased, yielding a (9s2p)/[5s2p] set. Tests using the B3LYP method, fixed experimental structures, and a more extended (10s2p)/[6s2p] Li set yielded a mean difference in shift of only 11 ppm, acceptably small in comparison with the mean Li shift of 201 ppm, where the means were computed over the five Li sites considered. The smaller (9s2p)/[5s2p] Li set is therefore used in all subsequent BS-II calculations. An Ahlrichs DZP-derived (double-ζ plus polarization) set[68] was applied for Fe, removing the most diffuse s and p shell, and increasing the exponent of the next most diffuse s shell, yielding a (13s9p5d)/[7s5p3d] set. Munzarová and Kaupp[66] further supplemented the DZP Fe functions with a diffuse (1s2p1d) set drawn from the effective core pseudopotential valence basis of Dolg et al.,[69] but this was not possible in the present calculations due to ensuing SCF instabilities. Numerical difficulties of this type are often encountered when attempting to apply molecular BSs bearing diffuse functions directly within periodic calculations. We note, however, that the proper basis for an infinite crystal comprises a series of Bloch functions, within which low exponent primitives might reasonably be neglected (in close-packed solids, at least), for we need never describe the decay of the electron distribution into vacuum.[62]

Spin-polarized hybrid exchange-correlation functionals based upon the B3LYP form[70−72] and bearing weights of Fock exchange $F_0 = 0\%$ (pure DFT), 20% (B3LYP), and 35% were applied. The B3LYP functional has previously demonstrated superior performance in reproducing the properties of a wide range of transition metal compounds,[73−76] while the $F_0 = 35\%$ functional has been shown to provide magnetic coupling constants in good agreement with experiment.[77,78] Again, the motivation here is to examine the ability of a range of functionals to reproduce the experimental hyperfine data. Sufficient convergence in total energies and spin densities was obtained by application of integral series truncation thresholds of 10^{-7}, 10^{-7}, 10^{-7}, 10^{-7} and 10^{-14} for Coulomb overlap and penetration, exchange overlap, and **g**- and **n**-series exchange penetration,

(59) Moskvin, A. S.; Ovanesyan, N. S.; Trukhtanov, V. A. *Hyperfine Interact.* **1977**, *3*, 429.
(60) Moskvin, A. S.; Ovanesyan, N. S.; Trukhtanov, V. A. *Hyperfine Interact.* **1977**, *5*, 13.
(61) Menetrier, M.; Rougier, A.; Delmas, C. *Solid State Commun.* **1994**, *90*, 439.
(62) Dovesi, R.; Saunders, V. R.; Roetti, C.; Orlando, R.; Zicovich-Wilson, C. M.; Pascale, F.; Civalleri, B.; Doll, K.; Harrison, N. M.; Bush, I. J.; D'Arco, P.; Llunell, M. *CRYSTAL06*; University of Torino: Torino, Italy: 2006.
(63) http://www.crystal.unito.it.
(64) Corno, M.; Busco, C.; Civalleri, B.; Ugliengo, P. *Phys. Chem. Chem. Phys.* **2006**, *8*, 2464.
(65) Merawa, M.; Labeguerie, P.; Ugliengo, P.; Doll, K.; Dovesi, R. *Chem. Phys. Lett.* **2004**, *387*, 453.
(66) Munzarová, M.; Kaupp, M. *J. Phys. Chem. A* **1999**, *103*, 9966.
(67) Kutzelnigg, W.; Fleischer, U.; Schindler, M. *NMR-Basic Principles and Progress*; Springer-Verlag, Heidelberg, 1990; Vol. 23.
(68) Schäfer, A.; Horn, H.; Ahlrichs, R. *J. Chem. Phys.* **1992**, *97*, 2571.
(69) Dolg, M.; Wedig, U.; Stoll, H.; Preuss, H. *J. Chem. Phys.* **1987**, *86*, 866.
(70) Becke, A. D. *J. Chem. Phys.* **1993**, *98*, 5648.
(71) Lee, C.; Yang, W.; Parr, R. G. *Phys. Rev. B* **1988**, *37*, 785.
(72) Miehlich, B.; Savin, A.; Stoll, H.; Preuss, H. *Chem. Phys. Lett.* **1989**, *157*, 200.
(73) Corà, F.; Alfredsson, M.; Mallia, G.; Middlemiss, D. S.; Mackrodt, W. C.; Dovesi, R.; Orlando, R. *Struct. Bonding (Berlin)* **2004**, *113*, 171.
(74) Mackrodt, W. C.; Middlemiss, D. S.; Owens, T. G. *Phys. Rev. B* **2004**, *69*, 115119.
(75) Middlemiss, D. S.; Wilson, C. C. *Phys. Rev. B* **2008**, *77*, 155129.
(76) Muscat, J.; Wander, A.; Harrison, N. M. *Chem. Phys. Lett.* **2001**, *342*, 397.
(77) Feng, X.; Harrison, N. M. *Phys. Rev. B* **2004**, *70*, 092402.
(78) Moreira, I. d. P. R.; Illas, F.; Martin, R. L. *Phys. Rev. B* **2002**, *65*, 155102.

respectively, along with isotropic Monkhorst−Pack reciprocal space meshes with shrinking factors 6, 6, 4, 4, 5, 5, 6, and 6 for heterosite $FePO_4$, $LiFeP_2O_7$, monoclinic and rhombohedral $Li_3Fe_2(PO_4)_3$, strengite, DH strengite, phosphosiderite, and DH phosphosiderite, respectively, where the parameters are all as described in the code documentation.[62]

Hyperfine calculations using the BS-II sets were performed within both the fixed experimental (termed a single point energy, denoted SPE) and the fully geometry optimized (atomic positions and lattice vectors; denoted OPT) structures. The optimizations used the BS-I sets and were pursued until convergence tolerances of 10^{-7}, 0.0003, and 0.0012 au for total energy, root-mean-square (rms) force, and rms displacement, respectively, were simultaneously satisfied. Tolerances for maximum force and displacement components were set at 1.5 times the respective rms values. All calculations assume a ferromagnetic spin distribution, as enforced by initial spin constraints on the cells consistent with five unpaired electrons per Fe(III) site. We note, however, that the final total energies and spin and charge distributions are obtained in the absence of such constraints. The charge and spin density distributions within the cells were further analyzed by application of the Mulliken partitioning scheme.[79]

The isotropic chemical shifts at ^{31}P and ^{7}Li sites are assumed to be dominated by the Fermi contact (FC) interaction with Hamiltonian (see Supporting Information for a complete derivation)

$$H_{FC} = \frac{2}{3}\mu_0\mu_B\mu_N g_e g_I |\psi^{\alpha-\beta}(\mathbf{R}_N)|^2 \mathbf{I}\cdot\mathbf{S} \quad (3)$$

where **I** denotes the nuclear spin angular momentum vector operator [with quantum numbers $I = 1/2$ and 3/2 for ^{31}P and ^{7}Li, respectively, and g_I values of 2.26322 and 2.170977, respectively.[80] **I** is quantized along the axis defined by the applied static induction, $\mathbf{B}_0$, taken here to lie along the z axis. The component along this axis is given by quantum number m_I (in units of $\hbar$), where m_I takes the values $-I, -I+1,..., I-1, I$]; **S** is the electron spin angular momentum vector operator [treated analogously to **I** above, with quantum number $S = 1/2$ and components along the $\mathbf{B}_0$||z axis (in units of $\hbar$) given by $m_S = \pm 1/2$]; $|\psi^{\alpha-\beta}(\mathbf{R}_N)|^2$ is the spin-unpaired electron density at the position $\mathbf{R}_N$ of the NMR observed nucleus. The latter quantity represents the sole explicit contribution of the DFT calculations to E_{FC}. A convenient physical model of the interaction involves the penetration of an amount $-Vg_e\mu_B\mathbf{S}|\psi^{\alpha-\beta}(\mathbf{R}_N)|^2$ of electronic moment into the nuclear volume V, where it experiences an assumed uniform magnetic flux density $\mathbf{B} = 2\mu_0 g_I \mu_N \mathbf{I}/3V$ due to the nuclear magnetic moment.

The $\mathbf{B}_0$ fields applied here are sufficiently high that we may treat the hyperfine interactions within the uncoupled regime, so that H_{FC} then operates upon states defined by good quantum numbers $|ISm_Im_S\rangle$ and the factor $\mathbf{I}\cdot\mathbf{S}$ occurring in H_{FC} may be replaced with the operator product I_zS_z. The first-order energy shift due to H_{FC} is then $\langle ISm_Im_S|H_{FC}|ISm_Im_S\rangle$, yielding hyperfine-split energy levels $A_{iso}m_Im_S$ where

$$A_{iso} = \frac{2}{3}\mu_0\mu_B\mu_N g_e g_I |\psi^{\alpha-\beta}(\mathbf{R}_N)|^2 \quad (4)$$

is the isotropic hyperfine coupling constant appearing in eq 1. The selection rules $\Delta m_I = \pm 1$ and $\Delta m_S = 0$ defining the present single quantum NMR experiments lead to a hyperfine energy splitting $A_{iso}/2$ (in addition to the normal nuclear Zeeman splitting) separating the initial and final states of the allowed NMR transitions. In a form equivalent to eq 1, the isotropic shift (ppm) associated with the Fermi contact interaction is then straightforwardly obtained as

$$\delta_{iso} = \frac{10^6 A_{iso}\Phi}{2h\nu_0} \quad (5)$$

where $\Phi = M_{para}/M_{sat}$ denotes the magnetization scaling factor (derived below) relating the saturated ferromagnetic magnetization, M_{sat}, represented by the DFT calculations to the much weaker paramagnetic magnetization, M_{para}, relevant to the NMR experiments. Note that eq 1 is not used directly here, for it does not include the scaling just discussed.

The electron−nuclear magnetic dipolar (dip) interactions are also computed, where the associated anisotropic hyperfine coupling tensor is of the form

$$\mathbf{A}^{ij}_{dip} = -\frac{\mathbf{T}_{ij}}{4\pi}\mu_0\mu_B\mu_N g_e g_I \quad (6)$$

where i and j label Cartesian axes. The elements of the symmetric dipolar tensor **T** at a given nuclear position take the integral form

$$\mathbf{T}_{ij} = \sum_{\mu\nu}\sum_{\mathbf{g}} P^{\alpha-\beta}_{\mu\nu\mathbf{g}} \int \varphi_\mu(\mathbf{r}) \frac{r^2\Delta_{ij} - 3r_ir_j}{r^5} \varphi^{\mathbf{g}}_\nu(\mathbf{r}) d\mathbf{r} \quad (7)$$

in which P denotes the direct space spin density matrix, μ and ν label atomic orbitals [φ_μ in the reference cell ($\mathbf{g} = 0$) and $\varphi^{\mathbf{g}}_\nu$ in the **g**th cell], **g** spans the set of lattice vectors, **r** denotes a position vector originating at the NMR observed nucleus, and Δ_{ij} denotes the Kronecker delta (capitalized to differentiate it from the shift, δ). Here, the **T** tensor represents the sole explicit contribution of the DFT calculations to $\mathbf{A}^{ij}_{dip}$. Note that eqs 6 and 7 above bear close analogy with a sum over the pairwise dipolar interactions of the observed nuclear moment with each of an array of electronic moments distributed throughout the lattice. Clearly, the present DFT calculations yield the electron spin density as a continuous scalar field, necessitating the integral form for $\mathbf{T}_{ij}$ adopted in eq 7, but previous studies have made useful progress by considering the unpaired electrons to be completely localized in the form of point dipoles situated at TM nuclear positions.[81,82] As for the FC interaction, the NMR selection rules lead to a hyperfine energy splitting $\mathbf{A}^{ij}_{dip}/2$ (again in addition to the nuclear Zeeman splitting) separating initial and final states of the allowed NMR transitions, the shifts (ppm) associated with the principal tensor components being obtained as

$$\delta_{kk} = \frac{10^6 \mathbf{A}^{kk}_{dip}\Phi}{2h\nu_0} \quad (8)$$

(79) Mulliken, R. S. *J. Chem. Phys.* **1955**, *23*, 1833.
(80) Weil, J. A.; Bolton, J. R.; Wertz, E. *Electron Paramagnetic Resonance-Elementary Theory and Practical Applications*; John Wiley: New York, 1994.
(81) Lee, Y. J.; Grey, C. P. *J. Phys. Chem. B* **2002**, *106*, 3576.
(82) Nayeem, A.; Yesinowski, J. P. *J. Chem. Phys.* **1988**, *89*, 4600.

Table 1. Summary of the Experimental Effective Magnetic Moments, μ_{eff} (μ_B), and Weiss Constants, Θ (K), Used in the Hyperfine Calculations and Fe and P Site Total Unpaired Electron Populations and Relative Static Energies of Polymorphic Forms Obtained from the BS-I $F_0 = 20\%$ Full Structural Optimizations

	heterosite[109]	rhombohedral $Li_3Fe_2(PO_4)_3$[22]	monoclinic $Li_3Fe_2(PO_4)_3$[22]	$LiFeP_2O_7$[47]	strengite	phosphosiderite	DH strengite	DH phosphosiderite
				experimental susceptibility data				
μ_{eff} (μ_B)	6.125	5.77	5.89	5.89	5.86	5.74	5.92[e]	5.92[e]
Θ (K)	−390	−50	−55	−73	−42.3	−45.8	−97.9[e]	−147.9[e]
				total Mulliken unpaired electron populations ($F_0 = 20\%$, BS-I, optimized cells)[a]				
$n^{\alpha-\beta}$(Fe)	4.279	4.294, 4.319	4.289, 4.296	4.315	4.306	4.315	4.209	4.248
$n^{\alpha-\beta}$(P)	0.017	0.020	all 0.020	0.022, 0.016	0.022	0.021	0.029	0.029
				relative energies of polymorphic forms ($F_0 = 20\%$, BS-I, optimized cells)				
E_{rel} (kJ/mol)	0[b]	+11.4[c]	0[c]		0[d]	+1.1[d]	+8.1[b]	+4.9[b]

[a] Li unpaired electron populations too small to be accurately extracted from Mulliken analyses. [b] $FePO_4$ polymorphs. [c] $Li_3Fe_2(PO_4)_3$ polymorphs. [d] $FePO_4 \cdot 2H_2O$ polymorphs. [e] See Supporting Information.

where $k = x, y, z$ corresponds to a principal axis of the diagonalized **T** tensor, the components arranged such that $|\delta_{zz}| \geq |\delta_{xx}| \geq |\delta_{yy}|$ and naturally obeying the traceless condition $\delta_{zz} + \delta_{xx} + \delta_{yy} = 0$. The dipolar width, defined as $|\delta_{zz} - \delta_{xx}|$, is later compared with the experimental spectral widths.

For ^{7}Li sites, the widths of the spinning sideband manifolds due to the first-order quadrupole interaction are also computed, where, for $I = 3/2$, the upper and lower edges of the satellite transitions are separated in frequency by

$$C_Q = \frac{eQV_{zz}}{h} \tag{9}$$

in which Q denotes the ^{7}Li electric quadrupole moment of 0.0401 barns[83] and V_{zz} the largest principal component of the diagonalized traceless electric field gradient tensor obtained from the DFT calculations. The relative importance of the dipolar and quadrupolar interactions in determining the observed spectral widths is discussed below.

In deriving an expression for the scaling factor, $\Phi = M_{para}/M_{sat}$, we first note that this might normally be assumed equal to the Brillouin function, $B_J(\lambda)$, for a species with total electronic angular momentum quantum number J[84]

$$B_J(\lambda) = \frac{2J+1}{2J}\coth\left(\frac{2J+1}{2J}\lambda\right) - \frac{1}{2J}\coth\left(\frac{\lambda}{2J}\right) \tag{10}$$

where

$$\lambda = \frac{g_J\mu_B J B_0}{k_B(T-\Theta)} \tag{11}$$

and in which g_J denotes the Landé g factor, k_B the Boltzmann constant, and Θ the experimentally determined Weiss constant of the compound considered. However, a further approximation is made here to more readily incorporate the fact that the experimental effective moment and the spin-only moment represented by the DFT calculations typically differ. Noting that the quotient λ is typically much smaller than unity, we follow the derivation of the Curie law and substitute the Maclaurin expansion for coth(x), yielding $B_J(\lambda) \approx (J+1)\lambda/3J + O(\lambda^3)$. Retaining only the term linear in λ and noting that the present DFT calculations neglect the orbital angular momentum [likely to be small for Fe(III)], so that a value $J \equiv S_{form}$ (the formal spin of the TM species) may be assumed in the expression for M_{sat}, the scaling factor for each material is obtained as

$$\Phi(B_0,T,\Theta,S_{form},\mu_{eff}) = \frac{B_0\mu_{eff}^2}{3k_B g_e \mu_B S_{form}(T-\Theta)} \tag{12}$$

where μ_{eff} is the experimental effective moment obtained along with Θ from fits of the Curie−Weiss law to the experimental $\chi^{-1}(T)$ curves. A value $S_{form} = 5/2$ is used for Fe(III) hereafter, along with the experimentally derived μ_{eff} and Θ values presented in Table 1. A temperature of $T = 320$ K is also assumed throughout, partly to account for the effects of frictional heating in the ^{7}Li MAS experiments. The factor Φ for each material is used directly in eqs 5 and 8 above. A detailed derivation of Φ is presented in the Supporting Information.

The potential disadvantages and sources of error arising within this method are apparent. First, it must be regarded as semiempirical, relying as it does upon data derived from experimental susceptibility measurements. Second, implicit throughout is the assumption that the pointwise paramagnetic magnetization in the lattice may be reasonably approximated by an isotropic scaling of the ferromagnetic magnetization. Third, no account has been taken of the effects of magnetic anisotropy (giving rise to the 'pseudocontact' shift) and zero-field splitting (ZFS) upon the hyperfine parameters. The former requires explicit knowledge of the second-rank $\boldsymbol{\chi}$ or **g** tensor and the latter the second-rank **g** tensor and ZFS D value. Such effects are expected to be significantly smaller than the dominant interactions treated above [in particular, the anisotropy in $\boldsymbol{\chi}$ for a d^5 TM ion such as Fe(III) will be small or nonexistent]: the reviews of Bertini et al.[56] and Kaupp and Köhler[85] provide further discussion.

4. Experimental Methods

4.1. Sample Preparation. Strengite (orthorhombic $FePO_4 \cdot 2H_2O$) was prepared by mixing 0.009 M $FeCl_3 \cdot 6H_2O$ and 0.027 M H_3PO_4 solutions under magnetic stirring.[19] The pH of the mixed solution was adjusted to 3 by addition of 0.04 M NaOH solution, and the final solution was refluxed for 2 days. A yellowish powder of strengite was obtained following centrifugation and drying at room temperature. A portion of the synthesized material was dried for 12 h at 140 °C, leading to the formation of the DH strengite phase.[19]

Phosphosiderite (monoclinic $FePO_4 \cdot 2H_2O$) was synthesized by mixing 0.009 M $FeCl_3 \cdot 6H_2O$ and 0.027 M H_3PO_4 solutions, adjusting the pH to approximately 1 by addition of 0.5 M HCl solution.[19] The resulting solution was refluxed for 12 days and the phosphosiderite solid product separated from the mother liquor by centrifugation followed by drying at room temperature. A portion of the synthesized material was dried at 80 °C for 12 h under vacuum, forming the associated DH phosphosiderite phase.[7] The

(83) Pyykkö, P. *Mol. Phys.* **2008**, *106*, 1965.
(84) Blundell, S. J. *Magnetism in Condensed Matter*; Oxford University Press, Oxford, U.K., 2001.
(85) Kaupp, M.; Köhler, F. H. *Coord. Chem. Rev.* **2009**, *253*, 2376.

preparations of monoclinic and rhombohedral $Li_3Fe_2(PO_4)_3$ and of $LiFeP_2O_7$ are described in refs 8, 9, 12, 21−23, and 86.

4.2. Characterization. 4.2.1. X-ray Diffraction (XRD) and Magnetic Susceptibility Measurements. XRD data (see Supporting Information) were collected for all samples on a Rigaku Miniflex diffractometer using Cr Kα radiation. Following conversion to the 2θ values appropriate for Cu Kα radiation, the XRD patterns of DH strengite and DH phosphosiderite samples were compared directly with the previously reported patterns.[7,19] Similarly, the XRD patterns of strengite, phosphosiderite, monoclinic and rhombohedral $Li_3Fe_2(PO_4)_3$ compounds, and $LiFeP_2O_7$ were compared with patterns simulated on the basis of the previously reported structural refinements of these compounds.[9,11,46,48]

The magnetic characterizations of strengite and phosphosiderite were performed using a Quantum Design MPMS XL-5 SQUID magnetometer. The temperature-dependent DC susceptibilities [$\chi(T) = M(T)/H$, where M is the sample magnetization and H the applied static magnetic field] were measured while cooling the sample from 300 to 2 K in a static magnetic field of 1000 Oe. The Curie and Weiss constants, C and Θ, respectively, were obtained from linear fits to the $\chi^{-1}(T)$ data. In addition, field-cooled (FC) and zero-field-cooled (ZFC) susceptibilities were measured from 300 to 2 K in a magnetic field of 10 Oe. The susceptibility data obtained previously[7] for DH strengite and DH phosphosiderite were also reanalyzed, the results being presented in the Supporting Information.

4.2.2. Solid-State NMR. ^{31}P ($I = 1/2$) spin−echo mapping experiments were performed on a CMX-200 spectrometer equipped with a 5 mm Chemagnetics static probe at a Larmor frequency of approximately 81 MHz. The ^{31}P NMR spectra were referenced to an 85% wt H_3PO_4 solution at 0 ppm. The experiments used a spin−echo pulse sequence of the form $90°_x$−τ−$180°_y$−τ−acquire with an evolution period τ of 20 μs and a 90° pulse width of 3 μs. The irradiation frequency was varied with a step size of 0.08 MHz over ranges as large as 2 MHz, where the step size was chosen to be less than ω_1,[87] a separate spectrum being collected at each irradiation frequency. The individual (phased) spectra were then summed, after addition of an appropriate offset frequency, to yield the full spectrum. We note that this methodology, termed 'spin−echo mapping' by some[52−54,87−90] and 'VOCS' (variable offset cumulative spectrum) by others,[91−93] is required in order to uniformly excite resonance(s) the line width of which is greater than the bandwidth and excitation profile of the probe, a condition met by many of the ^{31}P resonances observed here. Such a technique is particularly important if the dipolar width and the center of gravity of a static spectrum are to be extracted with any accuracy.

The spin−lattice relaxation (T_1) times were measured by use of an inversion−recovery pulse sequence. A pulse delay of 0.01 s was used on the basis of the measured T_1 time of approximately 0.5 ms for strengite. The T_1 times of the other compounds were assumed to be similar or shorter. The electron−nuclear dipolar couplings arising within the ^{31}P NMR spectrum of $LiFeP_2O_7$, the only compound within which appreciably asymmetric line shapes were observed, were simulated using the MATNMR module within MATLAB V.7.1,[94] yielding the isotropic resonances.

^{31}P spin−echo MAS NMR experiments for monoclinic $Li_3Fe_2(PO_4)_3$ alone were performed at 11.7 and 4.7 T on Varian Infinity Plus and CMX-200 spectrometers equipped with Samoson 1.3 and 1.8 mm MAS probes, respectively, at Larmor frequencies of approximately 202 and 81 MHz, respectively. The evolution period τ of the spin−echo pulse sequence was synchronized with the spinning speed. A 90° pulse width of 1.15 μs and a pulse delay of 0.05 s were used to acquire the 11.7 T data, while a 90° pulse width of 1.50 μs and a pulse delay of 0.05 s were used for the 4.7 T data. ^{31}P MAS NMR spin−echo mapping experiments, again for monoclinic $Li_3Fe_2(PO_4)_3$ alone, were performed at 11.7 T with an irradiation frequency step size of 0.2 MHz over a 2 MHz range, where the step size was chosen to be less than ω_1 (0.22 MHz). A pulse delay of 0.05 s was used.

The ^7Li ($I = 3/2$) MAS (magic angle spinning) NMR experiments were performed at a Larmor frequency of 77.7 MHz on a CMX-200 spectrometer equipped with a Chemagnetics 3.2 mm HFX MAS probe. Spinning speeds in the range 17−20 kHz were used, a 1.0 M LiCl solution at 0 ppm being adopted as a reference. A rotor-synchronized spin−echo pulse sequence with a pulse delay of 0.15 s and a pulse width of 3.3 μs was used.

5. Results and Discussion

5.1. Powder XRD and Magnetic Susceptibility Measurements. The XRD powder patterns of as-synthesized strengite, phosphosiderite, and their anhydrous phases are in good agreement with the previously reported data[7,19] (Figure S1, Supporting Information). Similarly, the $LiFeP_2O_7$ and monoclinic and rhombohedral $Li_3Fe_2(PO_4)_3$ samples yield XRD powder patterns similar to those simulated on the basis of the previously reported crystal structures[9,11,46] (Figure S2, Supporting Information).

The field-cooled and zero-field-cooled (FC and ZFC) susceptibility curves of strengite both show broad peaks at approximately 6−7 K (Figure 2a), indicating the onset of magnetic order. The FC curve of strengite reveals an increase in magnetic susceptibility below the ordering temperature typical of a ferrimagnetic material. The susceptibility follows the Curie−Weiss law above this temperature, a fit of the form $\chi = \chi_o + C/(T - \Theta)$, yielding μ_{eff} and Θ values of 5.86 μ_B and −42.3 K, respectively. Meanwhile, phosphosiderite displays a magnetic phase transition in the range 21−25 K (Figure 2b), fits of the Curie−Weiss form yielding μ_{eff} and Θ values of 5.74 μ_B and −45.8 K, respectively, as presented in Table 1. Phosphosiderite also shows ferrimagnetic ordering, with S-shaped susceptibility curves apparent below the transition. The Curie−Weiss parameters obtained from refitting of the DH strengite and DH phosphosiderite χ(T) curves (Section S4, Supporting Information) are also presented in Table 1.

5.2. Solid-State NMR. 5.2.1. ^{31}P NMR. The static solid-state NMR spectra of the Fe(III) phosphates presented in Figures 3−5 yield extremely large ^{31}P contact shifts in the approximate range 5700−20500 ppm, with broad spectral widths amounting, in some cases, to more than 4000 ppm. It is noted that many of these resonances are too broad to allow a simple determination of the isotropic resonance even by use of ultrafast MAS (typically >50 kHz), as discussed in more detail later for the case of monoclinic $Li_3Fe_2(PO_4)_3$. The majority of the resonances display near symmetric line shapes within which the peak maxima lie very close to the center of gravity, so that the former may be taken as a close approximation to the value of the isotropic resonance. However, the line shapes of both resonances in $LiFeP_2O_7$ are clearly asymmetric, the positions of the isotropic resonances therefore being estimated by spectral simulations in this case. Analysis of the spectrum of monoclinic $Li_3Fe_2(PO_4)_3$ presents greater challenges, as discussed below. The large shifts may be generally ascribed to the FC interaction described above,

(86) Rousse, G.; Rodriguez-Carvajal, J.; Wurm, C.; Masquelier, C. *Appl. Phys. A: Mater. Sci. Process.* **2002**, *74*, S704.
(87) Tong, Y. Y. *J. Magn. Reson., Ser. A* **1996**, *119*, 22.
(88) Sananes, M. T.; Tuel, A.; Volta, J. C. *J. Catal.* **1994**, *145*, 251.
(89) Sananes, M. T.; Tuel, A.; Volta, J. C. *J. Catal.* **1994**, *148*, 395.
(90) Canesson, L.; Boudeville, Y.; Tuel, A. *J. Am. Chem. Soc.* **1997**, *119*, 10754.
(91) Massiot, D.; Farnan, I.; Gautier, N.; Trumeau, D.; Trokiner, A.; Coutures, J. P. *Solid State Nucl. Magn. Reson.* **1995**, *4*, 241.
(92) Ash, J. T.; Grandinetti, P. J. *Magn. Reson. Chem.* **2006**, *44*, 823.
(93) Schurko, R. W.; Wi, S.; Frydman, L. *J. Phys. Chem. A* **2002**, *106*, 51.
(94) van Beek, J. D. *J. Magn. Reson.* **2007**, *187*, 19.

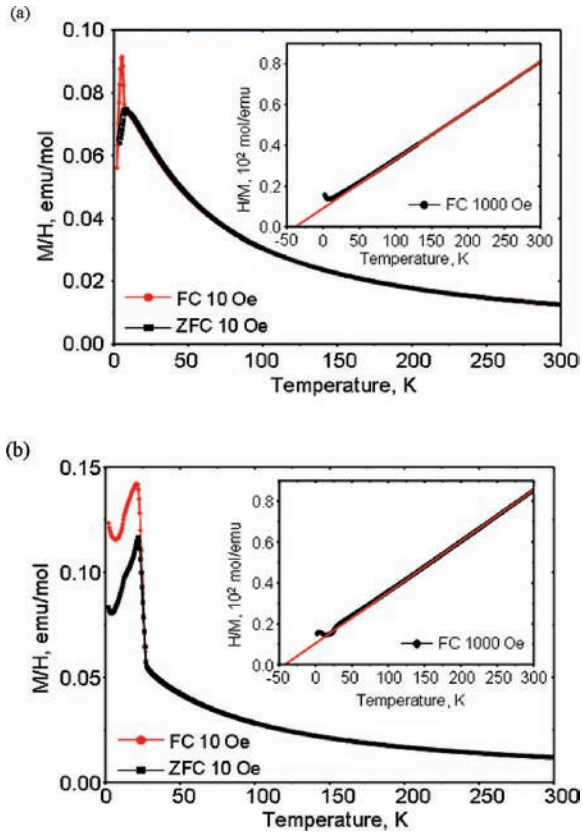

Figure 2. FC and ZFC molar susceptibility curves of (a) strengite and (b) phosphosiderite in a 10 Oe field. Insets: linear fits to the reciprocal molar susceptibilities obtained in a 1000 Oe field.

typical ^{31}P chemical shifts for diamagnetic phosphate phases lying in the approximate range ±100 ppm.[95] The broad line widths, meanwhile, may be directly attributed to electron−nuclear dipolar interactions, on the basis that ^{31}P is a spin-1/2 nucleus and therefore experiences no quadrupolar coupling and that typical chemical shift anisotropies in other phosphate phases amount to less than 100 ppm.[96−104]

Heterosite $FePO_4$ displays one isotropic resonance at 5770 ppm under MAS conditions (spectrum not shown, see ref 105). A peak maximum at 14 350 ppm is observed for rhombohedral $Li_3Fe_2(PO_4)_3$ (Figure 3a), while strengite and DH strengite yield peak maxima at 15 800 and 20 426 ppm, respectively (Figure 3b and 3c) and phosphosiderite and DH phosphosiderite at 16 680 and 19 149 ppm, respectively (Figure 3d and 3e). Each of these six compounds bears only one symmetry unique P site, as discussed above.[7,10,46] The number of observed ^{31}P NMR resonances is consistent with the crystallographic data in each case. The magnitudes of the hyperfine shifts increase in the order heterosite < rhombohedral $Li_3Fe_2(PO_4)_3$ < strengite < phosphosiderite < DH phosphosiderite < DH strengite. The relevant structural details are reported in Table 2.

Mindful of the simple Fe−O−P bond angle based model (eq 2) described in section 3.1 above, it is difficult to rationalize the ordering of the shifts on the basis of any single factor listed in Table 2. Consider, for example, that the compound with the largest number of Fe−O−P contacts displays the smallest shift. However, a generally increasing trend is evident with opening of the average Fe−O−P angle and with contraction of the average bond distance, both of these factors possibly explaining the smaller shift obtained for heterosite $FePO_4$. The results of the contact shift calculations performed within the fixed experimental structures (SPE), presented in Table 3, reproduce the experimental order, save that the DH phosphosiderite and DH strengite values are transposed. However, the calculations using the fully optimized (OPT) structures further transpose the strengite and phosphosiderite shifts. More detailed comparisons of the experimental and theoretical shifts follow below.

Static spin−echo mapping provides three peak maxima at 14 230, 15 250, and 16 200 ppm for monoclinic $Li_3Fe_2(PO_4)_3$ (Figure 4a), consistent with the number of symmetry-distinct P sublattices discussed above.[11] The P2, P1s, and P1 sites display average Fe−O distances of 1.97, 2.04, and 2.01 Å, respectively, all with average P−O bond lengths of 1.53 Å.[11] On this basis, the peaks at 14 230, 15 250, and 16 200 ppm are assigned to P1s, P1, and P2 sites, respectively. Here, examination of the average Fe−O−P bond angles for each site does not aid the assignment, given that these span a narrow range of 2.6° around an overall average of 144.7°. The calculations (Table 3) confirm the proposed experimental shift assignments in all methods applied. However, the experimental peak separations δ_{iso}(P1) − δ_{iso}(P1s) and δ_{iso}(P2) − δ_{iso}(P1s) of 1020 and 950 ppm, respectively, are only qualitatively reproduced by the SPE calculations: values of 632 and 536 ppm, respectively, are obtained at F_0 = 0%; 651 and 617 ppm, respectively, at F_0 = 20%; and 622 and 563 ppm, respectively, at F_0 = 35%. The F_0 = 20% OPT method performs significantly more poorly, yielding values of 449 and 277 ppm, respectively. However, some of the apparent discrepancies likely arise out of the fact that the resonances overlap in this phase, leading to greater uncertainty in the positions of the isotropic shifts relative to the peak maxima.

In light of these discrepancies and given that monoclinic $Li_3Fe_2(PO_4)_3$ represents the most challenging of the materials studied, we attempted exploratory ^{31}P MAS experiments for this phase alone. The spin−echo mapping MAS spectra (Figure 4b) acquired at spinning frequencies of 50, 53, 55, and 58 kHz in an 11.7 T field clearly reveal the most serious challenge, namely, that even over a narrow range of spinning frequencies the peak positions vary significantly due to the interplay of the variations in temperature associated with frictional heating and the relative motion in the spinning sideband positions arising directly out of the variations in spinning speed. As a consequence, it is very difficult to unambiguously identify the isotropic resonances. The problem is compounded by the broad line widths of the individual spinning sidebands (approximately 22−32 kHz for

(95) MacKenzie, K. J. D.; Smith, M. E. *Multinuclear Solid-State Nuclear Magnetic Resonance of Inorganic Materials*; Pergamon Materials Series; Pergamon: Elmsford, NY, 2002; Vol. 6.
(96) Fry, R. A.; Kwon, K. D.; Komarneni, S.; Kubicki, J. D.; Mueller, K. T. *Langmuir* **2006**, *22*, 9281.
(97) He, H.; Klinowski, J. *J. Phys. Chem.* **1993**, *97*, 10385.
(98) Moreno-Real, L.; Maldonado-Manso, P.; Leon-Reina, L.; Losilla, E. R.; Mouahid, F. E.; Zahir, M.; Sanzc, J. *J. Mater. Chem.* **2002**, *12*, 3681.
(99) Amine, K.; Yasuda, H.; Yamachi, M. *J. Power Sources* **1999**, *81*−*82*, 221.
(100) Nakayama, H.; Eguchi, T.; Nakamura, N.; Yamaguchi, S.; Danjyo, M.; Tsuhako, M. *J. Mater. Chem.* **1997**, *7*, 1063.
(101) Pinheiro, T. J. T.; Watts, A. *Biochemistry* **1994**, *33*, 2451.
(102) Rothwell, W. P.; Waugh, J. S.; Yesinowski, J. P. *J. Am. Chem. Soc.* **1980**, *102*, 2637.
(103) Tropp, J.; Blumenthal, N. C.; Waugh, J. S. *J. Am. Chem. Soc.* **1983**, *105*, 22.
(104) Zeyer, M.; Montagne, L.; Kostoj, V.; Palavit, G.; Prochnow, D.; Jaeger, C. *J. Non-Cryst. Solids* **2002**, *311*, 223.
(105) Cabana, J.; Shirakawa, J.; Cheng, G.; Richardson, T. J.; Grey, C. P. *Chem. Mater.* **2010**, *22*, 1249.

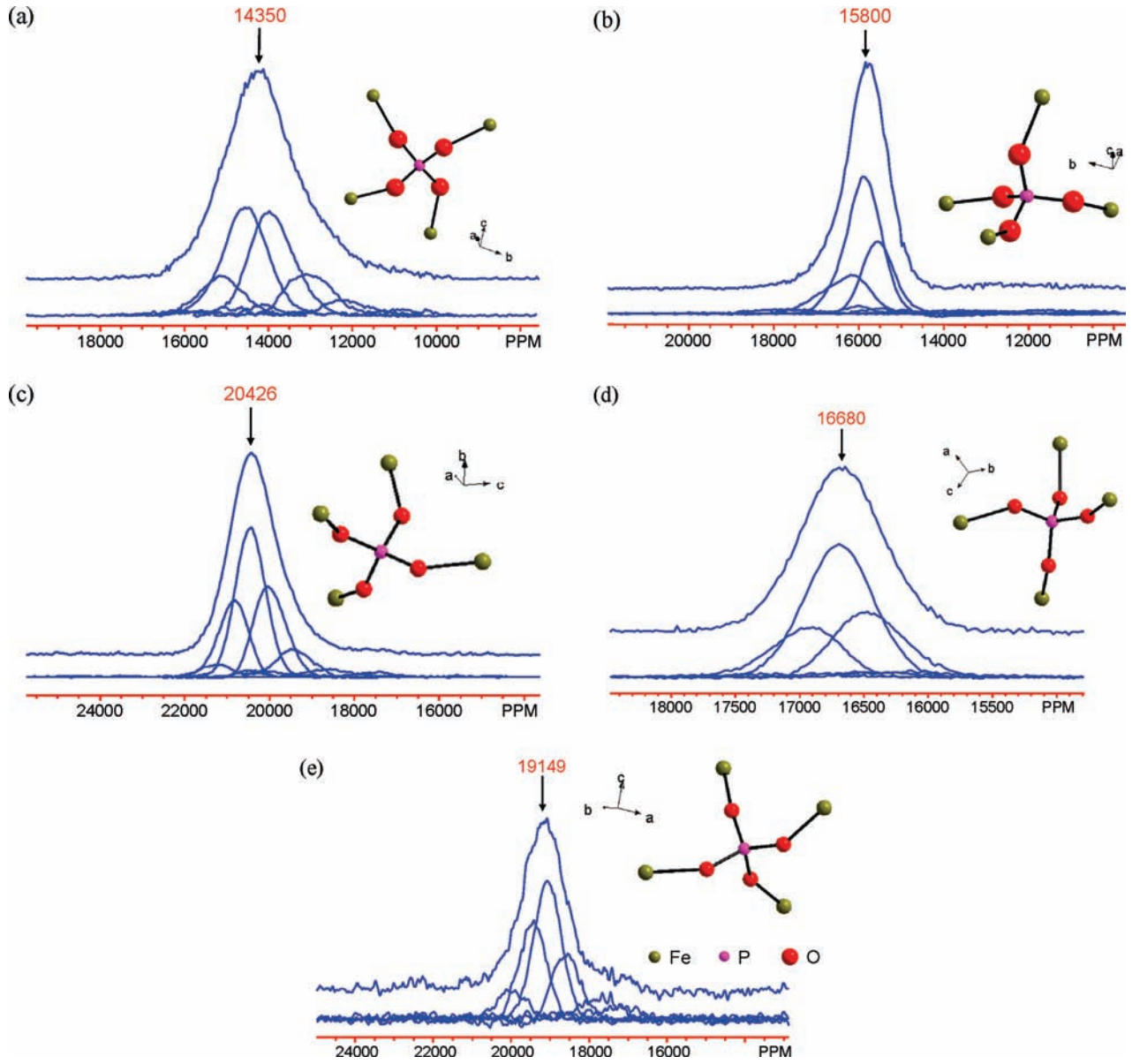

Figure 3. Spin−echo mapping ^{31}P NMR spectra of (a) rhombohedral $Li_3Fe_2(PO_4)_3$, (b) strengite, (c) DH strengite, (d) phosphosiderite, and (e) DH phosphosiderite. In these and all subsequent ^{31}P spectra, the individual subspectra collected at different offsets are shown below and their sum above. Insets: the local environments of P ions.

this sample, the exact value depending upon the field strength). However, by identifying at least one isotropic resonance and tracking the position of this isotropic peak as a function of spinning frequency, it is possible to effectively scale and align the MAS spectra obtained at each spinning frequency onto a selected reference spectrum, thereby negating the effects of frictional heating. The method is fully described in the Supporting Information; Figure 4c shows the final MAS spectra at 11.7 T (58 kHz) and 4.7 T (38 kHz) scaled and aligned using the static spin−echo mapping spectrum as reference. Three isotropic resonances at 14 514, 15 401, and 16 235 may be unambiguously identified from the combined spectra, assigned to the P1s, P1, and P2 sites, respectively, as above and leading to peak separations $\delta_{iso}(P1) - \delta_{iso}(P1s)$ and $\delta_{iso}(P2) - \delta_{iso}(P1s)$ of 887 and 834 ppm, respectively. The latter values are in marginally better agreement with the calculated separations presented above.

The line shape simulations for $LiFeP_2O_7$ shown in Figure 5 provide two isotropic resonances at 8230 and 14 398 ppm, again consistent with the number of inequivalent P sublattices determined crystallographically.[8,9,47] The reported crystal structure yields longer average Fe−O and similar average P−O bond distances for the P2 site (2.02 and 1.51 Å, respectively) as compared with the P1 site (1.96 and 1.51 Å, respectively).[9] The same sites show significantly different average Fe−O−P bond angles at 132.8° and 139.3°, respectively. Assuming that both angles lie above the putative shift minimum at $\theta = \cos^{-1}(-\beta/2\gamma)$ (see eq 2), so that an increase in angle leads to increased shift, the peaks at 8230 and 14 398 ppm can reasonably be assigned to P2 and P1 sites, respectively. The calculations (Table 3) confirm this assignment in all methods. Furthermore, the experimental shift separation of 6168 ppm is well reproduced, values of 7401, 6278, 5643, and 7070 ppm being obtained from the F_0 = 0%, 20%, and 35% SPE and F_0 = 20% OPT calculations, respectively.

5.2.2. Correlation of Experimental and Theoretical ^{31}P NMR Parameters. Table 3 and Figure 6 compare the experimental [MAS isotropic shifts for monoclinic $Li_3Fe_2(PO_4)_3$] and

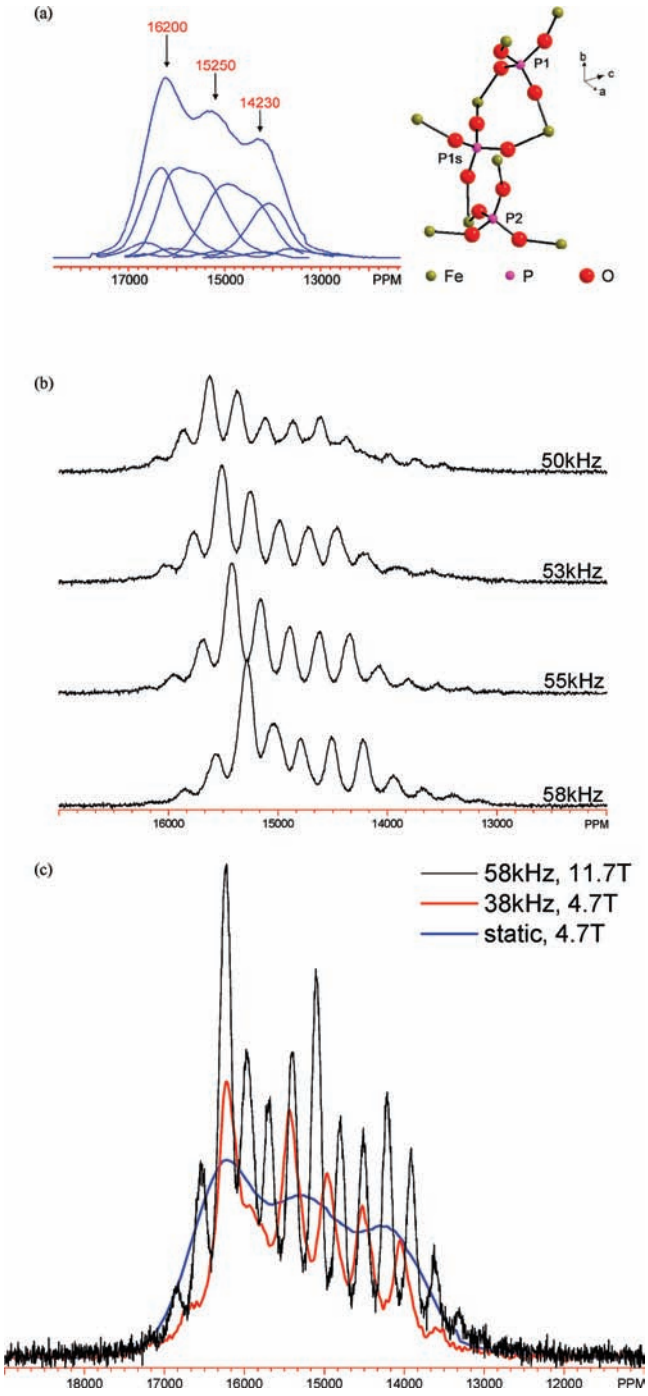

Figure 4. ^{31}P NMR spectra of monoclinic $Li_3Fe_2(PO_4)_3$: (a) Static spin−echo mapping spectrum at 4.7 T. Inset: the local environments of P ions. (b) Spin−echo mapping MAS spectra at 11.7 T with spinning frequencies of 50, 53, 55, and 58 kHz. (c) Comparison of the spin−echo mapping MAS spectrum at 11.7 T (58 kHz spinning frequency), spin−echo MAS spectrum at 4.7 T (38 kHz spinning frequency), and static spin−echo mapping spectrum, the former two scaled to be consistent with the latter.

theoretical ^{31}P NMR parameters. Examining first the two sets of SPE $F_0 = 20\%$ data, it is clear that the inclusion of residual magnetic correlations, as embodied within the Curie−Weiss model, leads to markedly superior agreement with experiment. Application of a Curie-type model, in which μ_{eff} is set to the spin-only value of 5.92 μ_B and Θ to zero, leads to much larger deviations, where it is apparently the omission of accurate Θ values that dominates. It is clear that future theoretical studies of hyperfine interactions in related materials must incorporate

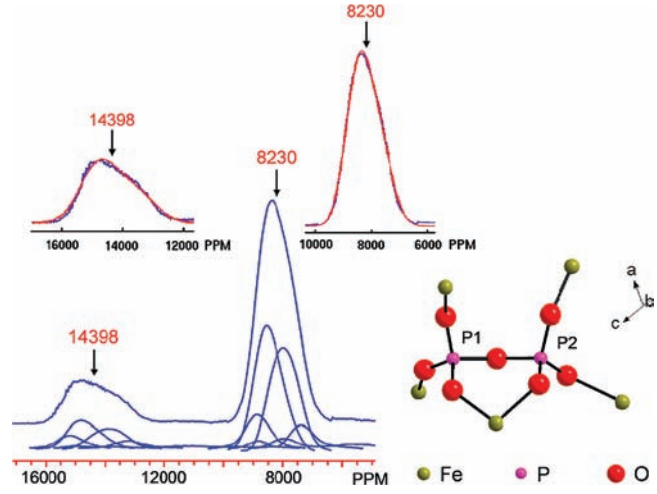

Figure 5. Spin−echo mapping ^{31}P NMR spectrum of $LiFeP_2O_7$. Insets: the local environments of P ions and isotropic resonance positions estimated by simulations of the respective line shapes.

such effects, ideally deriving the relevant magnetic parameters from first principles. Parameterization of Θ on the basis of the total energies of a range of magnetic configurations would seem to offer a promising initial prospect. We note also that the previous DFT study of hyperfine effects in a range of TM oxide cathodes did not fully account for the variations in susceptibilities across the phases considered, although the Weiss constants of many, but not all, of the materials considered were small.[41]

Second, it is evident that the hyperfine shifts depend strongly on the Fock exchange content of the Hamiltonian: $F_0 = 0\%$ (pure DFT) overestimating and the $F_0 = 35\%$ method underestimating the experimental shifts. This is consistent with the well-known trend whereby the amount of spin density delocalized from TM to ligand sites increases progressively as F_0 is reduced,[73] due mainly to the concomitant decrease in the strength of the electron pair interactions. Similar effects underlie the equally well-established trend whereby the exchange coupling between TM ions increases in strength as F_0 is reduced.[73,78] The dipolar interactions are apparently less affected by change of functional, indicating that the relatively small redistributions of spin density (conserving the total number of unpaired electrons per cell) accompanying variations in F_0 are not of marked consequence for dipolar effects.

Table 3 also presents the calculated rms errors (rmses) and Pearson correlation coefficients, the former serving as an approximate measure of confidence in the computed results in that sites characterized by hyperfine shifts the separations of which are less than the respective rmse value might be incorrectly identified (save in the case that the errors are mainly systematic in nature). All of the calculations yield high correlation coefficients close to unity. However, comparing rmse values, it is clear that the $F_0 = 20\%$ SPE and OPT calculations yield a superior set of shifts, the fitted lines shown in Figure 6 corresponding to $\delta_{iso,calc} = 1.094\delta_{iso,expt} - 1040$ ppm in the former case and $\delta_{iso,calc} = 1.005\delta_{iso,expt} + 155$ ppm in the latter. On the basis of a gradient very close to unity and the low rmse value and intercept, it is argued that the accuracy of the $F_0 = 20\%$ OPT set is superior, providing an overall excellent level of agreement with experiment.

Comparison of the experimental and theoretical dipolar widths is hampered by the fact that the experimental spectra are subject to additional sources of broadening from bulk magnetic

Table 2. Summary of the Average Fe−O−P Bond Angles, Fe−O and O−P Bond Distances, and Number of Fe−O−P Contacts Taken from the Reported Crystallographic Structures,[7,10,46,48] Together with the Observed ^{31}P Hyperfine Shifts

	average ∠(Fe−O−P) (deg)	average *d*(Fe−O) (Å)	average *d*(O−P) (Å)	no. of Fe−O−P contacts	^{31}P shift (ppm)
heterosite	119.36	2.017	1.533	6	5770
rhombohedral $Li_3Fe_2(PO_4)_3$	143.24	2.006	1.535	4	14 350
strengite	139.02	1.968	1.535	4	15 800
phosphosiderite	144.40	1.956	1.528	4	16 680
DH phosphosiderite	148.80	1.886	1.531	4	19 149
DH strengite	138.69	1.854	1.534	4	20 426

susceptibility effects.[106] The strength of the effect is not simple to estimate, and importantly here, the resulting spectral profile can no longer be described by a single second rank tensor, the broadening often obscuring the underlying asymmetry of the line shape.[106] A reasonable approximation is therefore adopted in which the computed dipolar widths $|\delta_{zz} - \delta_{xx}|$ are compared with the full experimental widths measured at half peak maximum (fwhm), facilitating the calculation of correlation coefficients. In the case of the monoclinic $Li_3Fe_2(PO_4)_3$ phase, the width is measured at the half-maximum of the central peak. As shown in Table 3, the dipolar correlations are high for all theoretical methods, and it emerges that the rmse values are low, although no real significance can be attached to the latter in light of the presence of the broadening discussed above.

Table 1 also presents the Fe and P site unpaired electron counts, $n^{\alpha-\beta}$, obtained from Mulliken analyses of the final BS-I $F_0 = 20\%$ OPT wave functions. It is found that the Fe moments are all of the same approximate magnitude, varying over a relatively narrow range from 4.209 to 4.319 unpaired electrons, supporting the notion that a generally similar Fe(III) state persists across all compounds. There is apparently no correlation, however, between the experimental μ_{eff} and theoretical $n^{\alpha-\beta}$(Fe) values, in keeping with the understanding that the deviations of μ_{eff} from the spin-only Fe(III) value of 5.92 μ_B are likely due to the mixing in of higher lying terms of lower spin multiplicity or to more subtle effects of ordering not fully captured by the fitted Weiss constant. However, it is found that the $n^{\alpha-\beta}$(P) values track the computed shifts in an acceptable fashion, supporting the use of spin densities integrated over whole ions as a means by which to rationalize experimental contact shifts, albeit at a qualitative level. This is an important point given that the pseudopotential-based calculations commonly applied in the solid state do not routinely provide the spin densities at nuclear positions.

5.2.3. ^{7}Li MAS NMR. The $LiFeP_2O_7$ and rhombohedral $Li_3Fe_2(PO_4)_3$ structures each contain only one symmetry-distinct Li sublattice,[46,86] so that a single isotropic resonance is anticipated within the ^{7}Li MAS NMR spectra, occurring at 162 and 164 ppm, respectively (Figure 7a and 7b). The similarity of the shifts is consistent with the similarities in the Fe−O−Li bond path geometries in both compounds, the average Fe−O and Li−O distances and Fe−O−Li angles differing by only 0.01 Å, 0.01 Å, and 3.1°, respectively. The magnetic parameters of the two phases shown in Table 1 are also similar. Examining calculated values (Table 4), it is only the $F_0 = 20\%$ SPE method that reproduces the similarity of shifts in these two materials, the other approaches predicting larger peak separations.

Meanwhile, the three Li sublattices in monoclinic $Li_3Fe_2(PO_4)_3$[11] give rise to isotropic resonances at 40, 90, and 190 ppm (Figure 7c). Here, the Li1 and Li2 sites display four and the Li3 site three Li−O−Fe contacts within their first cation coordination shells, subject to the criterion that a substantive Li−O chemical bond should be shorter than 2.30 Å. The peak at 40 ppm is therefore assigned to the Li3 site, given that it experiences the smaller number of contacts to Fe sites. The Li1 site displays average Li−O and Fe−O distances of 1.96 and 2.04 Å and the Li2 site 2.00 and 2.08 Å, respectively.[11] On this basis, the Li1 and Li2 sites are assigned to the peaks at 190 and 90 ppm, respectively.

Our assignment differs from that reported by Davis et al.,[107] in which resonances at 102, 216, and 45 ppm were assigned to the Li1, Li2, and Li3 sites, respectively (where the Li site labels used by Davis et al.[107] have been amended here and hereafter to be consistent with the present scheme). The apparent discrepancy highlights the need to discriminate between Li−O contacts that are significant in terms of crystallography and lattice stability and those that might reasonably be expected to contribute to the Li contact shift. Davis et al. assign on the basis that the Li1, Li2, and Li3 sites are, respectively, 4-, 5-, and 5-fold O coordinated (in keeping with the crystallographic structure[11]) and that the Li2 site shows the strongest 90° and the Li3 site the weakest Li−O−Fe orbital overlaps.[107] However, as stated above, we contend that Li−O bonds of length significantly greater than the typical range 1.7−2.0 Å (1.996 Å in Li_2O)[108] are likely to be almost entirely electrostatic in character and will therefore convey little spin density to the terminal Li site. Thus, in terms of viable bond paths for contact shifts, the Li1, Li2, and Li3 sites are 4-, 4-, and 3-fold O coordinated, respectively, which, taken together with the mean Li−O and Fe−O bond lengths, leads to the assignment made above. Table S2 in the Supporting Information compares the local Li environments in the Patoux et al.[11] and Davis et al.[107] structures and the present and previous Li shift assignments.

The calculations (Table 4) confirm the present assignment in all methods, placing the Li1 site highest in shift, the Li3 site lowest, and the Li2 site at intermediate shift. However, the experimental $\delta_{\text{iso}}(\text{Li1}) - \delta_{\text{iso}}(\text{Li2})$ and $\delta_{\text{iso}}(\text{Li2}) - \delta_{\text{iso}}(\text{Li3})$ peak separations of 100 and 50 ppm, respectively, are only qualitatively reproduced by the calculations, with $F_0 = 0\%$ SPE values of 169 and 152 ppm, $F_0 = 20\%$ SPE values of 132 and 110 ppm, $F_0 = 35\%$ SPE values of 110 and 95, and $F_0 = 20\%$ OPT values of 158 and 27 ppm, respectively.

5.2.4. Correlation of Experimental and Theoretical ^{7}Li NMR Parameters. Examining the quality of agreement between the experimental and the theoretical ^{7}Li data presented in Table 4 and Figure 8, it is found that the shift correlation coefficients are all acceptably high. However, even the minimum shift rmse

(106) Grey, C. P.; Dobson, C. M.; Cheetham, A. K. *J. Magn. Reson.* **1992**, *98*, 414.
(107) Davis, L. J. M.; Heinmaa, I.; Goward, G. R. *Chem. Mater.* **2010**, *22*, 769.
(108) Bijvoet, J. M.; Claassen, A.; Karssen, A. *Proc. K. Ned. Acad. Wet.* **1926**, *29*, 1286.
(109) Yamada, A.; Takei, Y.; Koizumi, H.; Sonoyama, N.; Kanno, R. *Chem. Mater.* **2006**, *18*, 804.

Table 3. Experimental and Computed ^{31}P Hyperfine Shifts and Dipolar Widths [ppm; experimentally derived as full width at half-maximum (fwhm)] in the $F_0 = 0\%$, 20%, and 35% Hamiltonians for Both Fixed Experimental (SPE) and Optimized Geometries (OPT) Using the BS-II Atomic Sets[a]

^{31}P	site	δ_{iso} expt	δ_{iso}, $F_0 = 0\%$ SPE	δ_{iso}, $F_0 = 20\%$ SPE	δ_{iso}, $F_0 = 20\%$ SPE using χ_{Curie}	δ_{iso}, $F_0 = 35\%$ SPE	δ_{iso}, $F_0 = 20\%$ OPT	dipolar fwhm	$\lvert\delta_{zz} - \delta_{xx}\rvert$, $F_0 = 0\%$ SPE	$\lvert\delta_{zz} - \delta_{xx}\rvert$, $F_0 = 20\%$ SPE	$\lvert\delta_{zz} - \delta_{xx}\rvert$, $F_0 = 35\%$ SPE	$\lvert\delta_{zz} - \delta_{xx}\rvert$, $F_0 = 20\%$ OPT
heterosite $FePO_4$		5770	6269	4500	9315	3783	5563	1217	1305	1251	1227	1367
rhomb $Li_3Fe_2(PO_4)_3$		14 350	17 139	14 049	17 077	12 466	14 456	1839	1660	1459	1373	1878
strengite		15 800	19 308	15 364	17 730	13 612	16 234	1078	962	857	812	844
DH strengite		20 426	24 499	19 552	25 499	17 126	19 547	1263	773	796	784	545
phosphosiderite		16 680	20 114	16 264	19 750	14 508	14 699	742	351	309	329	496
DH phosphosiderite		19 149	27 078	22 169	32 373	19 642	20 648	1276	1720	1534	1401	1589
mono $Li_3Fe_2(PO_4)_3$	P1s	14 514^{MAS}	19 206	15 703	18 565	14 063	15 895	3029[b]	3176[c]	3077[c]	2875[c]	2764[c]
	P1	15 401^{MAS}	19 837	16 353	19 334	14 685	16 343					
	P2	16 235^{MAS}	20 373	16 970	20 063	15 249	16 620					
$LiFeP_2O_7$	P1	14 398	18 544	14 988	18 571	13 043	15 289	2147	2246	2329	1953	2232
	P2	8230	11 144	8710	10791	7400	8219	1460	1652	1561	1551	1557
$r_{Pearson}$			0.977	0.972	0.897	0.971	0.973		0.943	0.950	0.950	0.913
rmse			4208	1208	5259	1715	997		281	281	293	305

[a] Temperature set at 320 K, and effective magnetic moments and Weiss constants are as quoted in Table 1, save for values labeled χ_{Curie}, where $\mu_{eff} = \mu_{spin\text{-}only}(Fe^{III}) = 5.92\ \mu_B$ and $\Theta = 0$ K were applied. The Pearson correlation coefficients ($r_{Pearson}$) linking the experimental and theoretical sets and root mean square errors (rmse) in the computed values are also shown. [b] Upon the basis of the half-height of the P1 resonance. [c] Approximated as $[\delta_{iso}(P2) - \delta_{iso}(P1s)] + (1/2)[\delta_{zz}(P1s) - \delta_{xx}(P1s) + \delta_{zz}(P2) - \delta_{xx}(P2)]$. Values labeled MAS were obtained from ^{31}P MAS experiments.

Figure 6. Correlations of the calculated (BS-II basis sets) ^{31}P hyperfine shifts of Fe(III) phosphates for various Hamiltonians with experimental data. Solid lines denote linear fits. The dashed line shows the ideal trend $\delta_{iso,calc} = \delta_{iso,expt}$: (black circles) $F_0 = 0\%$ SPE ($\delta_{iso,calc} = 1.303\delta_{iso,expt} - 560$ ppm); (blue squares) $F_0 = 20\%$ SPE ($\delta_{iso,calc} = 1.094\delta_{iso,expt} - 1040$ ppm); (red triangles) $F_0 = 35\%$ SPE ($\delta_{iso,calc} = 0.988\delta_{iso,expt} - 1221$ ppm); (green diamonds) $F_0 = 20\%$ OPT ($\delta_{iso,calc} = 1.005\delta_{iso,expt} + 155$ ppm). MAS-derived shifts were used for monoclinic $Li_3Fe_2(PO_4)_3$ and the static spin−echo-mapping-derived values for all other materials.

of 41 ppm, as obtained from the $F_0 = 35\%$ SPE calculations, amounts to a substantial fraction of the total experimental range of 150 ppm. The least-squares fitted line for the latter method corresponds to $\delta_{iso,calc} = 1.283\delta_{iso,expt} - 71$ ppm: the comparatively large gradient and intercept indicating a significantly poorer performance for ^{7}Li sites than was obtained for ^{31}P above. However, as above, it is found that the shifts vary sensitively with choice of functional, being overestimated and underestimated within the $F_0 = 0\%$ (pure DFT) and $F_0 = 35\%$ SPE calculations, respectively. Again, the application of Curie-type susceptibilities within the $F_0 = 20\%$ SPE method leads to higher rmse values and lower correlation coefficients, further emphasizing the need for an accurate treatment of the magnetic susceptibilities.

Analysis of the spectral widths for ^{7}Li sites is complicated by the fact that the dipolar and quadrupolar interactions may both contribute significantly to the spinning sideband intensities. Table 4 therefore compares both the $|\delta_{zz} - \delta_{xx}|$ and the C_Q parameters with the experimental data; it emerges that both types of interactions produce spectral widths of near equivalent magnitudes. Again, the effects of spectral broadening render the rmse values meaningless, but it is clear that the correlation coefficients computed on the basis of the dipolar widths are significantly higher than for quadrupolar widths, leading us to suggest that dipolar interactions may dominate in the present materials. Experiments at varying static field strengths (or with ^{6}Li) would be needed to test this point further. It emerges that both types of interactions are relatively insensitive to the Fock exchange content of the functional. Note that ^{6}Li experiments were not pursued for the reason that ^{6}Li enrichment is generally required in order to obtain spectra of sufficient quality to allow detailed spectral analysis of the line shapes. The ^{7}Li experiments provide hyperfine shifts of sufficient accuracy for the present purposes, while the calculated dipolar and quadrupolar correlation coefficients show unambiguously that the former interactions dominate over the latter in determining the spectral width, as discussed above.

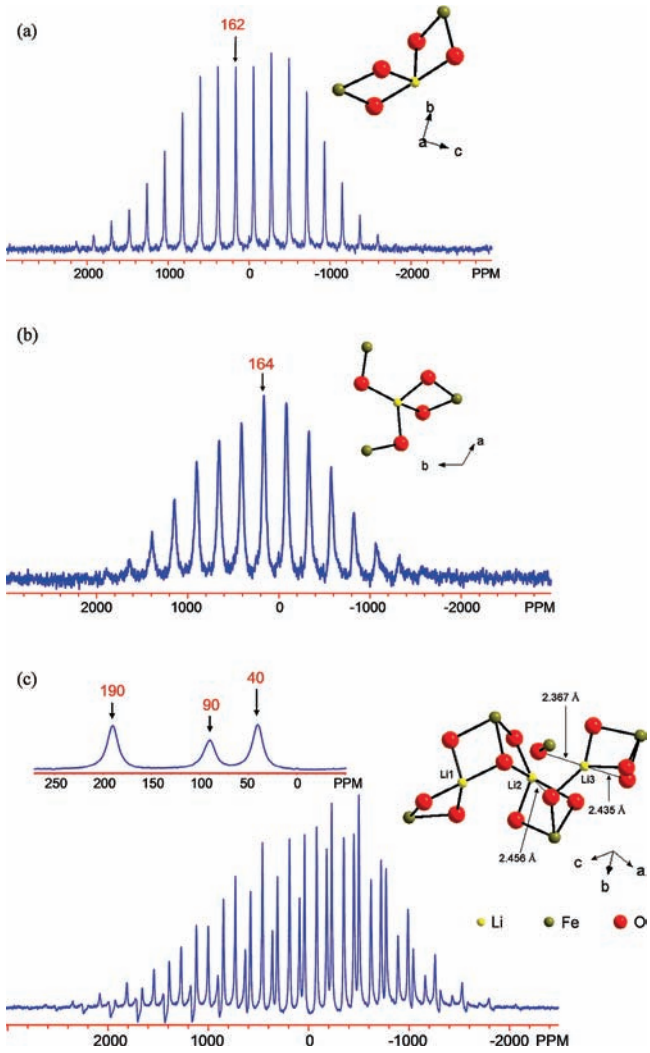

Figure 7. ^{7}Li MAS NMR spectra of (a) $LiFeP_2O_7$, (b) rhombohedral $Li_3Fe_2(PO_4)_3$, and (c) monoclinic $Li_3Fe_2(PO_4)_3$, all at a Larmor frequency of 77.7 MHz. The isotropic resonances are labeled with their hyperfine shifts. MAS speeds of 17, 21, and 19 kHz were used for $LiFeP_2O_7$, monoclinic $Li_3Fe_2(PO_4)_3$, and rhombohedral $Li_3Fe_2(PO_4)_3$, respectively. Insets: the local environments of lithium ions.

Although calculations on a wider range of model compounds are required, the present results suggest that the application of DFT-derived spin densities in support of paramagnetic $^{6/7}$Li NMR experiments may be of less assistance than for similar paramagnetic ^{31}P studies. It is of interest to consider the reasons why this may be so. Within the limits of the approach outlined, there is no readily apparent reason why the spin densities at Li nuclei should be inherently less accurate than those at P nuclei. However, a clear distinction does arise in relation to the lower mass of Li relative to P, which might be expected to lead to increased motion in the former case, possibly to the extent that the static calculations performed here might need to be replaced by some form of vibrational averaging of the hyperfine parameters. The amplitudes of motion of Li in the current materials might be further enhanced by the nature of the sites occupied, given that Li ions occupying voids or cages within rigid frameworks will likely experience lower average force constants than would P ions in PO_4 or P_2O_7 units. Future studies addressing vibrationally averaged hyperfine parameters will be of interest in regard to such issues. Furthermore, given that the ^{7}Li hyperfine shifts are much smaller in magnitude than the ^{31}P

Table 4. Experimental and Computed ^{7}Li Hyperfine Shifts and Spectral, Dipolar, and Quadrupolar Widths [ppm; experimentally derived as full width at half-maximum (fwhm)] in the $F_0 = 0\%$, 20%, and 35% Hamiltonians for Both Fixed Experimental (SPE) and Optimized Geometries (OPT) Using the BS-II Atomic Sets[a]

^{7}Li	site	δ_{iso} expt	δ_{iso}, $F_0 = 0\%$ SPE	δ_{iso}, $F_0 = 20\%$ SPE	δ_{iso}, $F_0 = 20\%$ SPE using χ_{Curie}	δ_{iso}, $F_0 = 35\%$ SPE	δ_{iso}, $F_0 = 20\%$ OPT	spectral fwhm	$\lvert\delta_{zz} - \delta_{xx}\rvert$, and C_Q $F_0 = 0\%$ SPE	$\lvert\delta_{zz} - \delta_{xx}\rvert$, and C_Q $F_0 = 20\%$ SPE	$\lvert\delta_{zz} - \delta_{xx}\rvert$, and C_Q $F_0 = 35\%$ SPE	$\lvert\delta_{zz} - \delta_{xx}\rvert$, and C_Q $F_0 = 20\%$ OPT
rhomb $Li_3Fe_2(PO_4)_3$		164	479	243	295	117	295	1768	2095	2191	2236	2327
									2317[d] (0.180)	2394[d] (0.186)	2458[d] (0.191)	2432[d] (0.189)
$LiFeP_2O_7$		162	416	247	305	151	213	2146	2062	2130	2169	2448
									2059[d] (0.160)	2111[d] (0.164)	2136[d] (0.166)	2420[d] (0.188)
mono $Li_3Fe_2(PO_4)_3$	Li1	190	548	297	351	174	302	2571[b]	2846[c]	2862[c]	2880[c]	2682[c]
	Li2	90	379	165	195	64	144		2586[d,e] (0.190, 0.154, 0.162)	2579[d,e] (0.198, 0.157, 0.165)	2593[d,e] (0.203, 0.159, 0.168)	2091[d,e] (0.154, 0.159, 0.142)
	Li3	40	227	55	64	−31	117		0.864	0.845	0.839	0.989
$r_{Pearson}$			0.950	0.989	0.814	0.977	0.928		0.539[d]	0.423[d]	0.320[d]	−0.897[d]
rmse			287	78	123	41	91		251	297	324	372
									321[d]	362[d]	399[d]	499[d]

[a] Temperature set at 320 K, and effective magnetic moments and Weiss constants are as quoted in Table 1, save for values labeled χ_{Curie}, where $\mu_{eff} = \mu_{spin\text{-}only}(Fe^{III}) = 5.92\ \mu_B$ and $\Theta = 0$ K were applied. The Pearson correlation coefficients ($r_{Pearson}$) connecting the experimental and theoretical sets and root mean square errors (rmse) in the computed values are also shown. [b] Upon the basis of the half-height of the Li2 resonance. [c] Approximated as $[\delta_{iso}(Li1) - \delta_{iso}(Li3)] + (1/2)[\delta_{zz}(Li1) - \delta_{xx}(Li1) + \delta_{zz}(Li3) - \delta_{xx}(Li3)]$. [d] Quadrupolar width [C_Q values (MHz) shown in parentheses]. [e] Approximated as $[\delta_{iso}(Li1) - \delta_{iso}(Li3)] + (10^6/2\nu_0)[C_Q(Li1) + C_Q(Li3)]$ (ppm).

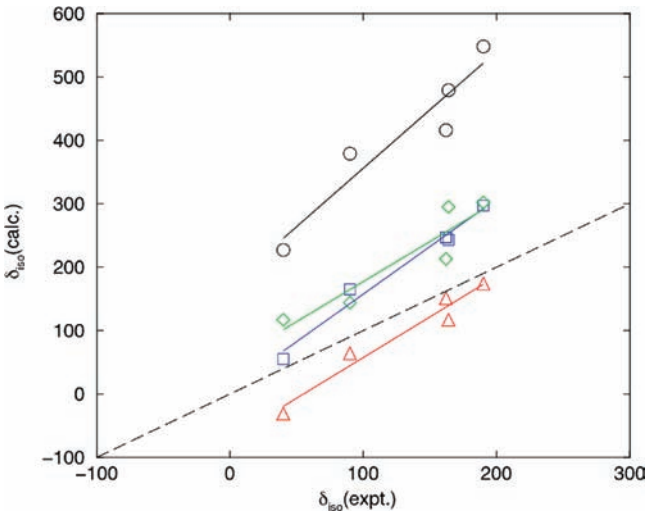

Figure 8. Correlations of the calculated (BS-II basis sets) ^{7}Li hyperfine shifts of Fe(III) phosphates for various Hamiltonians with the experimental data. Solid lines denote linear fits: (dashed line) ideal trend $\delta_{iso,calc} = \delta_{iso,expt}$; (black circles) $F_0 = 0\%$ SPE ($\delta_{iso,calc} = 1.843\delta_{iso,expt} + 172$ ppm); (blue squares) $F_0 = 20\%$ SPE ($\delta_{iso,calc} = 1.502\delta_{iso,expt} + 7$ ppm); (red triangles) $F_0 = 35\%$ SPE ($\delta_{iso,calc} = 1.283\delta_{iso,expt} - 71$ ppm); (green diamonds) $F_0 = 20\%$ OPT ($\delta_{iso,calc} = 1.262\delta_{iso,expt} + 51$ ppm).

values, additional contributions not explicitly included within the present DFT approach (e.g., the zero-field splitting and pseudocontact terms) might be expected to be more consequential.[85]

6. Conclusions

The present study constitutes an extensive investigation of the correlations linking the hyperfine NMR parameters and local environments of ^{7}Li and ^{31}P nuclei in a range of Fe(III) phosphate model compounds. In addition to experimental NMR analyses, complementary periodic DFT calculations of the relevant hyperfine and quadrupolar parameters have been performed. Hybrid functionals incorporating varying weights of nonlocal Fock exchange have been applied, together with an empirical model of the paramagnetic susceptibilities. The calculations not only confirm the assignments of ^{7}Li and ^{31}P resonances made on the basis of analyses of the crystal structures but also provide further insight into the sensitivity of hyperfine and quadrupolar parameters to the composition of the functional. The present approach also offers the advantage that the use of a range of Hamiltonians lends credence to those trends appearing consistently throughout.

The main finding is that a combined NMR experimental and theoretical approach to the hyperfine parameters characterizing the present class of Fe(III)-bearing magnetic materials is both practicable and highly useful. Methods of this type are uniquely placed to further establish the correlations linking contact shifts and electron−nuclear dipolar and quadrupolar tensors to the details of the local environments of the observed nuclei. More specifically, for DFT calculations, the rmse values and correlation coefficients obtained for ^{31}P sites from the $F_0 = 20\%$ SPE and OPT methods indicate accuracies sufficient to permit for the assignment of shifts to the inequivalent sublattices within the more structurally complex materials. This is particularly true when the method of assignment is broadened to include not only the contact shifts but also the relative spectral widths due to dipolar interactions. Similar conclusions hold for ^{7}Li sites, although the relative accuracy of the calculated shifts is somewhat lower, raising the need for further calculations on a wider range of model compounds. Here, the analysis of the spectral widths is further complicated by the potential contribution of both dipolar and quadrupolar interactions. The other significant findings are as follows. (i) The assignment of shifts on the basis of the number and geometry of Fe−O−P and Fe−O−Li bond pathways is reconfirmed as a useful albeit qualitative approach. (ii) The proposed scaling of the theoretical shifts computed within the ferromagnetic state on the basis of experimentally derived Curie−Weiss parameters is apparently effective and accurate. (iii) In contrast, the shifts computed using Curie-type susceptibilities, defined as the combination of an ideal Fe(III) spin-only effective moment with a Weiss constant of zero, provide markedly inferior agreement with experiment for both species. The omission of realistic Θ values dominates the effect, clearly demonstrating the need to account for the residual magnetic correlations manifesting within the paramagnetic state. Future work will examine the feasibility of deriving the parameters defining $\chi(T)$ directly from first-principles calculations. Parameterization of Θ on the basis of the total energies of a range of magnetic configurations offers a promising initial prospect. (iv) The variations in Fermi contact shifts with hybrid functional are in keeping with the generally acknowledged trend in which decreasing admixture of Fock exchange leads to the progressive delocalization of spin from TM to ligand sites.[73] The effects of variations in Fock exchange content upon the electron−nuclear dipolar and quadrupolar tensors are shown to be less significant. (v) The unpaired electron counts for P, $n^{\alpha-\beta}$(P), obtained from Mulliken analyses are found to track the experimental shifts, supporting the use of spin densities integrated over whole ions (straightforwardly obtainable from pseudopotential calculations) as a qualitative means by which to analyze experimental spectra. (vi) The consistent experimental and theoretical assignment of shifts to the three inequivalent Li sublattices in monoclinic A-type $Li_3Fe_2(PO_4)_3$ differs from that reported in the previous study by Davis et al.[107]

Applications of a similar approach to a range of Li-ion battery cathode phases are underway, with particular emphasis upon the hyperfine and quadrupolar parameters characterizing $^{6/7}$Li sites in partially charged and/or disordered phases, the $^{6/7}$Li and ^{31}P sites in TM olivine-type phosphates, and materials bearing mixed TM cations wherein the redox processes are not completely understood. Similarly, combined paramagnetic NMR and computational studies of the bonding of phosphate ions to the surfaces of Fe(III) oxyhydroxides are also in progress, motivated by the environmental ubiquity and importance of such reactions. The wider technical questions raised by the present study relate mainly to the effects of motion upon the hyperfine parameters. We propose to address this issue for a small number of model phases by combining normal vibrational mode calculations with mode-sampling techniques, so as to arrive at a set of vibrationally averaged contact shifts and dipolar and quadrupolar tensors.

Acknowledgment. The authors thank Prof. Dr. Martin Kaupp (Julius-Maximilians Universität Würzburg), Dr. Jordi Cabana-Jimenez (Lawrence Berkeley National Laboratory), and Dr. Junichi Shirakawa (DuPont Japan) for useful discussions. The collection of static spectra and DFT calculations were funded by U.S. National Science Foundation grants CHE-0021934 and CHE-1065905. The collection of MAS data and dipolar calculations were supported as part of the Northeastern Center for Chemical Energy Storage (NECCES), an Energy Frontier Research Center funded by the U.S.

Department of Energy, Office of Science, Office of Basic Energy Sciences, under Award Number DE-SC0001294. The authors thank the Management Committee of the Seawulf Cluster at SUNY Stony Brook for the provision of computational resources.

Supporting Information Available: Detailed derivations of hyperfine Hamiltonians and magnetization scaling factor, X-ray diffraction patterns of strengite, DH strengite, phosphosiderite, DH phosphosiderite, $LiFeP_2O_7$, and rhombohedral and monoclinic $Li_3Fe_2(PO_4)_3$; refitting of the magnetic susceptibilities of DH strengite and DH phosphosiderite; ^{31}P spin−echo MAS NMR spectrum of monoclinic $Li_3Fe_2(PO_4)_3$; comparison of the Li environments and present and previous isotropic resonance assignments in monoclinic $Li_3Fe_2(PO_4)_3$. This material is available free of charge via the Internet at http://pubs.acs.org.

JA102678R